

Magnetic Field Dependent Microwave Losses in Superconducting Niobium Microstrip Resonators

Sangil Kwon,^{1,2, a)} Anita Fadavi Roudsari,¹ Olaf W. B. Benningshof,^{1,2} Yong-Chao Tang,^{1,3} Hamid R. Mohebbi,⁴ Ivar A. J. Taminiau,⁵ Deler Langenberg,⁴ Shinyoung Lee,⁶ George Nichols,^{1,2} David G. Cory,^{1,7,8,9} and Guo-Xing Miao^{1,3}

¹⁾*Institute for Quantum Computing, University of Waterloo, Waterloo, Ontario N2L 3G1, Canada*

²⁾*Department of Physics and Astronomy, University of Waterloo, Waterloo, Ontario N2L 3G1, Canada*

³⁾*Department of Electrical and Computer Engineering, University of Waterloo, Waterloo, Ontario N2L 3G1, Canada*

⁴⁾*High Q Technologies LP, Waterloo, Ontario N2L 0A7, Canada*

⁵⁾*Neutron Optics LP, Waterloo, Ontario N2L 0A7, Canada*

⁶⁾*Samsung Electronics, 1 Samsungjeonja-ro, Hwaseong-si, Gyeonggi-do, 445-330, Republic of Korea*

⁷⁾*Department of Chemistry, University of Waterloo, Waterloo, Ontario N2L 3G1, Canada*

⁸⁾*Perimeter Institute for Theoretical Physics, Waterloo, Ontario N2L 2Y5, Canada*

⁹⁾*Canada Institute for Advanced Research, Toronto, Ontario M5G 1Z8, Canada*

(Dated: 27 June 2018)

We describe an experimental protocol to characterize magnetic field dependent microwave losses in superconducting niobium microstrip resonators. Our approach provides a unified view that covers two well-known magnetic field dependent loss mechanisms: quasiparticle generation and vortex motion. We find that quasiparticle generation is the dominant loss mechanism for parallel magnetic fields. For perpendicular fields, the dominant loss mechanism is vortex motion or switches from quasiparticle generation to vortex motion, depending on cooling procedures. In particular, we introduce a plot of the quality factor versus the resonance frequency as a general method for identifying the dominant loss mechanism. We calculate the expected resonance frequency and the quality factor as a function of the magnetic field by modeling the complex resistivity. Key parameters characterizing microwave loss are estimated from comparisons of the observed and expected resonator properties. Based on these key parameters, we find a niobium resonator whose thickness is similar to its penetration depth is the best choice for X-band electron spin resonance applications. Finally, we detect partial release of the Meissner current at the vortex penetration field, suggesting that the interaction between vortices and the Meissner current near the edges is essential to understand the magnetic field dependence of the resonator properties.

I. INTRODUCTION

Superconducting resonators have been studied for half a century and their importance has grown especially rapidly in the past decade, driven by increased interest in quantum information and quantum devices.^{1–14} Recently, there is a renewed interest in using superconducting resonators for magnetic resonance and therefore to use them in magnetic fields.^{13–35} Our interest is to develop a resonator for X-band electron spin resonance (ESR) of thin films. We desire to have a small mode volume and a homogeneous microwave magnetic field over the sample, and so we employ a microstrip geometry.³⁶ Such resonators have the potential to significantly increase the signal-to-noise ratio, if the resonator maintains a high quality factor in a modest DC magnetic field.

Maintaining a high quality factor is not straightforward in a magnetic field because of magnetic field depen-

dent microwave losses.^{36–49} The focus of this paper is to develop experimental methods to understand and characterize the magnetic field dependent loss mechanisms, quasiparticle generation and current-induced motion of vortices.

The quasiparticle loss induced by a magnetic field is determined by both the film quality (clean/dirty) and its thickness. Regarding the film quality, dirtier films have a higher Ginzburg–Landau (GL) parameter;⁵⁰ therefore, they survive in higher field. However, dirtier films have more scattering sites that makes them lossier. As for the film thickness, thinner films are less sensitive to a magnetic field parallel to the film because the Meissner current does not repel all of the penetrating magnetic field.⁵⁰ Another advantage of thin films is that, if the thickness of a thin film is comparable to or thinner than its GL coherence length, vortices are not easily created by a magnetic field parallel to the film. However, when the film is too thin its quality degrades because the surface oxide layer and lattice mismatch between the substrate and the film become more important.^{51,52}

There are two approaches to avoiding loss from

^{a)}Electronic mail: kwon2866@gmail.com

current-induced vortex motion: one is to suppress the vortex motion of existing vortices and the other is to shift vortex penetration to a higher field. Most studies on vortices in planar resonators have focused on reducing vortex motion, by introducing artificial pinning sites such as slots³⁸ or antidots.^{39–41} The other approach is enhancing a surface barrier which delays vortex penetration until the external field reaches a value above the lower critical field of the resonator. At this field, called the vortex penetration field, the surface barrier is fully suppressed.^{53–55} In this work, we focus on the role of the Bean–Livingston surface barrier at the edges of microstrips,⁵⁶ rather than on artificial pinning sites.

Our approach to understanding the loss is outlined in Fig. 1. We systematically characterized a set of superconducting niobium microstrip resonators with different film quality, film thickness, and strip width by measuring their resonance frequencies f and quality factors Q as a function of magnetic fields both parallel to the microwave current H_{\parallel} and perpendicular to the film H_{\perp} .

We theoretically calculate f and Q for each resonator as a function of magnetic field using standard models for the complex resistivity of superconductors: the two-fluid model incorporated with the time-dependent GL equations (when quasiparticle generation is the dominant loss mechanism) or the Coffey–Clem model (when vortex motion is dominant). By varying the parameters, which are used to model the complex resistivity (the parameters in parentheses in the leftmost boxes of Fig. 1), we match the theoretical f and Q to determine the loss parameters.

To calculate f and Q , the quasiparticle/vortex distribution, microwave current density distribution, and stored electromagnetic energy need to be calculated. The quasiparticle distribution is given by the time-dependent GL equations used for the complex resistivity; the vortex distribution is assumed to be uniform or to follow the critical state models, depending on cooling procedures. The microwave current density distribution and the electromagnetic energy are calculated using Maxwell’s equations and the London equations.

An essential step is to identify the dominant loss mechanism, either quasiparticle generation or vortex motion, for each experimental condition. Once the dominant loss mechanism is known, we can use the appropriate model to compute the complex resistivity. In this work, we introduce a plot of Q vs. f^{-2} , which represents the characteristic relation between the real and imaginary parts of the complex resistivity, as a general method for identifying the dominant loss mechanism (Sec. IV C).

One outcome of the approach described in this paper is that we observe an anomaly in the magnetic field dependence of the resonance frequency and interpret it as partial release of the Meissner current along the strip edges at the vortex penetration field, a phenomenon which has not been reported for superconducting resonators (Sec. IV B).

Finally, our approach allows us to propose design criteria for high quality factor planar resonators that are

suitable for ESR applications (Sec. V).

This paper is organized as follows. Section II introduces the theories used for the calculations. Section III describes the details of the resonators and the experimental conditions. Section IV presents results and analysis. Section V concludes the paper. Some technical details have been deferred to Supplementary Materials.

II. THEORY

A. Resonance Frequency and Quality Factor

Consider a microstrip line oriented along the z axis with its width along the x axis and thickness along the y axis. The dissipated power per unit length P_{diss} as a function of external magnetic field H is

$$P_{\text{diss}}(H) = \frac{1}{2} \int_{\text{sc}} \rho_1(x, y, H) |J_{\text{mw}}(x, y, \lambda(H))|^2 dx dy \quad (1)$$

where “sc” stands for “inside superconducting media”, ρ is the complex resistivity $\rho_1 + i\rho_2$, J_{mw} is the microwave current density, and λ is the magnetic field penetration depth.

There are many other sources of power loss, such as coupling to external circuits or two-level systems.^{1,36,57–59} We assume that these losses do not have a magnetic field dependence.

The stored electromagnetic energy per unit length U_{em} can be divided into two parts, the energy stored as an electromagnetic field U_{field} and the additional energy contribution U_{add} :

$$\begin{aligned} U_{\text{em}}(H) &= U_{\text{field}}(H) + U_{\text{add}}(H) \\ &= \frac{1}{2} \int_{\text{all}} \mu_0 |H_{\text{mw}}(x, y, \lambda(H))|^2 dx dy \\ &\quad + \frac{1}{2} \int_{\text{sc}} \frac{\rho_2(x, y, H)}{\omega} |J_{\text{mw}}(x, y, \lambda(H))|^2 dx dy \end{aligned} \quad (2)$$

where μ_0 is the vacuum permeability, H_{mw} is the microwave magnetic field strength, and $\omega/2\pi$ is the frequency of an applied electromagnetic field.

The quality factor provides a convenient measure of the loss as Q^{-1} :

$$\frac{1}{Q(H)} = \frac{P_{\text{diss}}(H)}{\omega U_{\text{em}}(H)} \approx \frac{P_{\text{diss}}(H)}{\omega U_{\text{field}}(H)}. \quad (3)$$

We make an approximation for the last term as $U_{\text{field}} \gg U_{\text{add}}$. Therefore, the magnetic field dependence of ρ_1 can be studied via measuring Q as a function of H .

In a microstrip resonator, the resonance frequency indicates the phase velocity of the microwave signal, which is proportional to \sqrt{L} , where L is the effective inductance per unit length. The quantity L is defined by $U_{\text{em}} = L|I|^2/2$, where I is the total current. Like U_{em} , L

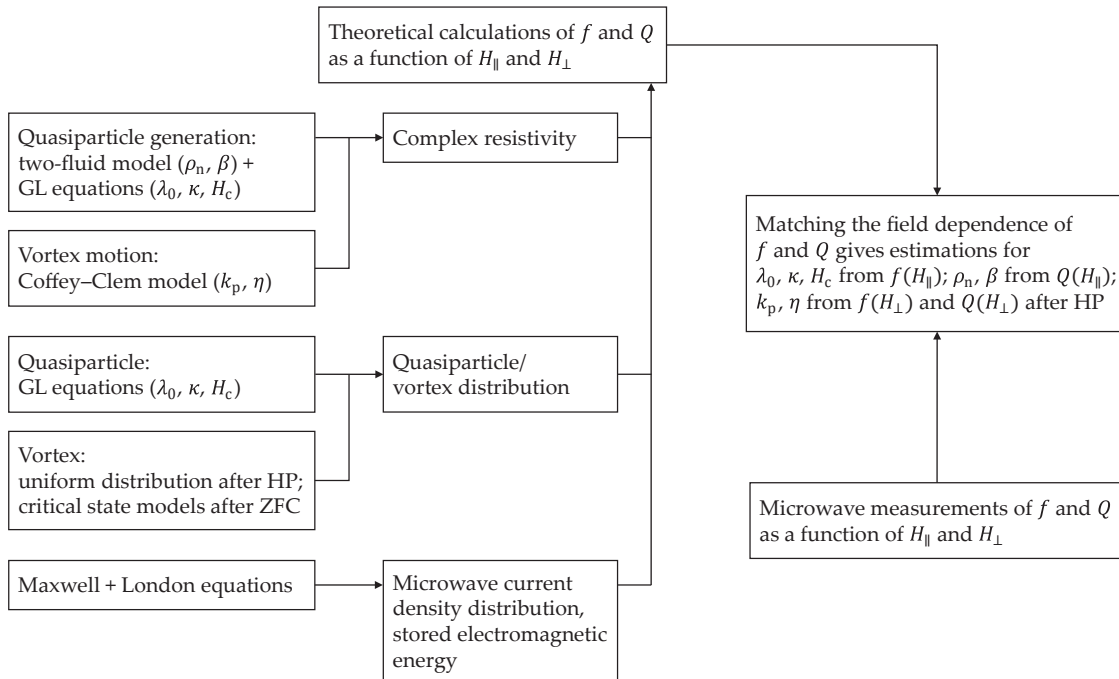


FIG. 1. Flow chart of our approach to characterize microwave losses induced by DC magnetic fields. Loss parameters, the parameters for modeling the complex resistivity, are in parentheses in the leftmost boxes. These are the zero-field penetration depth of the strip λ_0 , the GL parameter κ , the thermodynamic critical field H_c , the residual resistivity ρ_n , the exponent for the fraction of normal electrons in context of the two-fluid picture β (see Sec. II B 1), the restoring force constant of a pinning potential k_p , and the viscous drag coefficient associated with vortex motion η (see Sec. II B 2). ZFC and HP refer to zero-field cooling and heat-pulsing, respectively (see Sec. III).

has two terms:

$$L(H) = L_{\text{field}}(H) + L_{\text{add}}(H),$$

where L_{field} is the magnetic inductance from U_{field} , and L_{add} is an additional inductance from U_{add} . Hence,

$$L_{\text{field}}(H) = \frac{1}{|I|^2} \int_{\text{all}} \mu_0 |H_{\text{mw}}(x, y, \lambda(H))|^2 dx dy, \quad (4)$$

$$L_{\text{add}}(H) = \frac{1}{|I|^2} \int_{\text{sc}} \frac{\rho_2(H)}{\omega} |J_{\text{mw}}(x, y, \lambda(H))|^2 dx dy. \quad (5)$$

Given the assumption that the capacitance of a microstrip resonator is independent of magnetic field, the magnetic dependent part of L can be measured by the following equation:

$$\frac{f^{-2}(H) - f_0^{-2}}{f_0^{-2}} = \frac{L(H) - L_0}{L_0}, \quad (6)$$

where f_0 is the resonance frequency at zero-field, and L_0 is the effective inductance at zero-field. Hence, the magnetic field dependence of ρ_2 can be extracted from $f^{-2}(H)$.

The discussions so far suggest that we need ρ , J_{mw} , and U_{field} to calculate f^{-2}/f_0^{-2} and Q^{-1} as a function

of H . Among these, we can simulate J_{mw} and U_{field} by solving Maxwell's equations and the London equations (see Sec. S2). In the next subsection, we introduce several models for ρ .

B. Magnetic Field Dependent Loss Mechanisms

1. Quasiparticle Generation

When ω is low enough that $\omega\tau_{\text{qp}} \ll 1$, where τ_{qp} is the quasiparticle scattering time, the two-fluid model provides a convenient description of the complex conductivity due to the quasiparticle generation $\sigma_{\text{tf},1} - i\sigma_{\text{tf},2}$,⁵⁰

$$\sigma_{\text{tf},1} = \frac{n_n}{n_{\text{tot}}} \sigma_n, \quad (7)$$

$$\sigma_{\text{tf},2} = \frac{n_s e_s^2}{m_s \omega} = \frac{1}{\omega \mu_0 \lambda^2}, \quad (8)$$

where n_n is the local number density of normal electrons (quasiparticle), n_s is the local number density of superconducting electrons (Cooper pair), n_{tot} is the total number density of conduction electrons, σ_n is the inverse of ρ_n , e_s is the charge of a superconducting electron, m_s is the mass of a superconducting electron, and λ is the pene-

tration depth. The corresponding complex resistivity ρ_{tf} is given by $\rho_{\text{tf},i} = \sigma_{\text{tf},i}/(\sigma_{\text{tf},1}^2 + \sigma_{\text{tf},2}^2)$. As $\sigma_{\text{tf},1} \ll \sigma_{\text{tf},2}$ for the most of the magnetic field range, $\rho_{\text{tf},1}$ is approximately proportional to $\sigma_n \lambda^4$. Hence, for dirty superconductors, the number of scattering sites affects $\rho_{\text{tf},1}$ chiefly via their effect on λ .⁵⁰

In this work, n_s is calculated using the time-dependent GL equations in terms of the complex order parameter ψ :

$$n_s(x, y, H) = |\psi(x, y, H)|^2. \quad (9)$$

As the GL theory does not give n_n , we introduce an empirical expression for n_n with an additional exponent β :

$$\frac{n_n(H)}{n_{\text{tot}}} = \left[1 - \frac{n_s(H)}{n_s(0)} \right]^\beta. \quad (10)$$

This expression fits our data well (see Sec. IV A). For $\beta > 1$ ($\beta < 1$), n_n is less (greater) than that would be predicted by an ideal two-fluid model, $\beta = 1$. Thus the loss parameters associated with quasiparticle generation are $\sigma_n (=1/\rho_n)$, β , and parameters for the GL equations, λ_0 , κ , and H_c (see Sec. S1 for details on the GL equations).

2. Vortex Motion

Current-induced vortex motion is an important source of microwave dissipation. To describe the complex resistivity associated with vortex motion, we consider the interactions between pinning potentials and vortices. Among the several accepted models for this,^{60–63} we use the complex resistivity based on the Coffey–Clem model $\rho_{\text{CC},1} + i\rho_{\text{CC},2}$ given by⁶⁴

$$\rho_{\text{CC},i} \approx \rho_{\text{tf},i} + \rho_{\text{vm},i}, \quad (11)$$

where ρ_{vm} is the complex resistivity due to vortex motion. A useful property of Eq. (11) is that the total complex resistivity is the sum of ρ_{tf} and ρ_{vm} . Here, ρ_{vm} is given by^{63,64}

$$\begin{aligned} \rho_{\text{vm},1} &= \rho_{\text{ff}} \frac{(\omega/\omega_{\text{eff}})^2 + \epsilon}{1 + (\omega/\omega_{\text{eff}})^2}, \\ \rho_{\text{vm},2} &= \rho_{\text{ff}} \frac{\omega/\omega_{\text{eff}}(1 - \epsilon)}{1 + (\omega/\omega_{\text{eff}})^2}, \end{aligned} \quad (12)$$

where ω_{eff} is the characteristic frequency for vortex oscillations, which is linked to the depinning frequency ω_p and the creep parameter ϵ . ρ_{ff} is the flux-flow resistivity, the effective resistivity in the high frequency limit ($\omega \gg \omega_p$) where vortices flow freely,

$$\rho_{\text{ff}}(x, y, H_\perp) = \frac{\Phi_0}{\eta} B_\perp(x, y, H_\perp), \quad (13)$$

where Φ_0 is the magnetic flux quantum, B_\perp is the magnetic field perpendicular to the film inside the superconductor carried by vortices, and η is the viscous drag coefficient per unit vortex length associated with vortex motion. Here, the spatial distribution of vortices is given by $B_\perp(x, y, H_\perp)$.

In the temperature range we are interested in, $\lesssim 100$ mK, $\epsilon \rightarrow 0$ and $\omega_{\text{eff}} \rightarrow \omega_p$ (see Sec. S4 for justification); ω_p and η completely describe the complex resistivity from vortex motion. As ω_p is given by k_p/η , where k_p is the restoring force constant of a pinning potential per unit vortex length, the loss parameters associated with vortex motion are η and k_p .

A number of studies on the time-dependent GL equations showed that there are two different mechanisms for η : Tinkham mechanism and Bardeen-Stephen mechanism.^{50,65} If the material is an extreme type-II and the magnetic field is well below H_{c2} ($B_\perp \ll \mu_0 H_{c2}^\perp$), both mechanisms have the form

$$\rho_{\text{ff}} \approx \alpha_{\text{vm}} \rho_n \frac{B_\perp}{\mu_0 H_{c2}^\perp}, \quad (14)$$

where α_{vm} is a constant of order unity. By comparing Eqs. (13) and (14), we find

$$\eta \approx \frac{\mu_0 H_{c2}^\perp \Phi_0}{\alpha_{\text{vm}} \rho_n}. \quad (15)$$

A crucial property is that, according to Eq. (12), the dependence of $\rho_{\text{vm},1}$ and $\rho_{\text{vm},2}$ on B_\perp is the same. Hence if the field dependence of ρ_1 and ρ_2 is qualitatively different, it implies that quasiparticles, $\rho_{\text{tf},2}$, are the major contributors to ρ_2 . Note that also the loss contribution induced by excitations in a vortex core is a quasiparticle contribution.

To fully understand the microwave loss, we need to know the vortex distribution. The vortex distribution is determined by the cooling history and the pinning strength. For a sample cooled in a magnetic field (field cooling), vortices are homogeneously distributed regardless of the pinning strength, i.e., B_\perp in Eq. (13) becomes a constant. As a result, η and k_p can be obtained in a straightforward way.⁶⁶

For a sample cooled without a magnetic field (zero-field cooling), followed by turning on a magnetic field, we consider two extreme cases. If the critical current density associated with vortex pinning is much lower than the depairing current density (weak pinning limit), a high surface barrier exists and vortices accumulate near the center of the superconductor, called a vortex dome, due to the strong repulsive interaction between the Meissner current along edges and vortices.^{55,67–72} If the critical current density is comparable to the depairing current density (strong pinning limit), then vortices accumulate near the edges of the sample (Bean-type model).^{70,73,74} In this limit, the surface barrier is strongly suppressed by the pinning potentials.⁵⁴ For our resonators, the Bean–Livingston barrier is the dominant

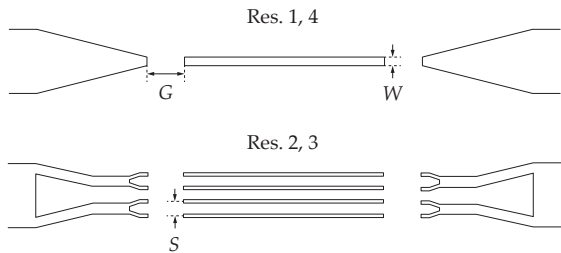


FIG. 2. Geometry of the resonators. Resonators 1 and 4 are single-strip resonators; resonators 2 and 3 are four-strip resonators.³⁶ G is the gap between the feedline and the resonator. W is the width of a strip. S is the spacing between center of strips. The values of G , W , and S are given in Table II.

surface barrier. The geometrical barrier is unimportant because the film thickness d is small enough to satisfy $d \lesssim \lambda \ll W$, where W is the width of the strips (see Tables II and III).

III. METHODS

Three double-side-polished $430 \mu\text{m}$ thick $2''$ diameter c -plane sapphire wafers were prepared and niobium films were grown by DC magnetron sputtering on both sides of the wafers. Then the resonators were fabricated by optical lithography and dry etching. (Details on the film growth and characterization are described in Sec. S5.) Table I summarizes the basic properties of films. The relation between T_c and ρ_n is similar to that reported in Refs. 51 and 52.

For this study, we chose a microstrip design made of straight half-wavelength resonators, as shown in Fig. 2, without any additional structures, such as antidots or slots. Res. 2 and 3 are multi-strip resonators. The working principle and performance of the multi-strip resonators can be found in Ref. 36. The dimensions and basic microwave properties of the resonators are shown in Table II.

Microwave measurements were performed in a dilution refrigerator (Leiden CF250). Schematic experimental configuration and cabling are shown in Fig. 3. Resonance frequency and quality factor were measured as a function of magnetic field by collecting full S -parameters using a vector network analyzer (Agilent N5230A). The resonance frequency f_{res} and the loaded quality factor Q_{load} were obtained by fitting the magnitude of the measured S_{21} to a complex Lorentzian function as follows:

$$|S_{21}(f)| = \left| \frac{S_{21,\text{max}}}{1 + i2Q_{\text{load}} \left(\frac{f}{f_{\text{res}}} - 1 \right)} + Ae^{i\phi} \right|, \quad (16)$$

where f is the excitation frequency, and $S_{21,\text{max}}$ is the

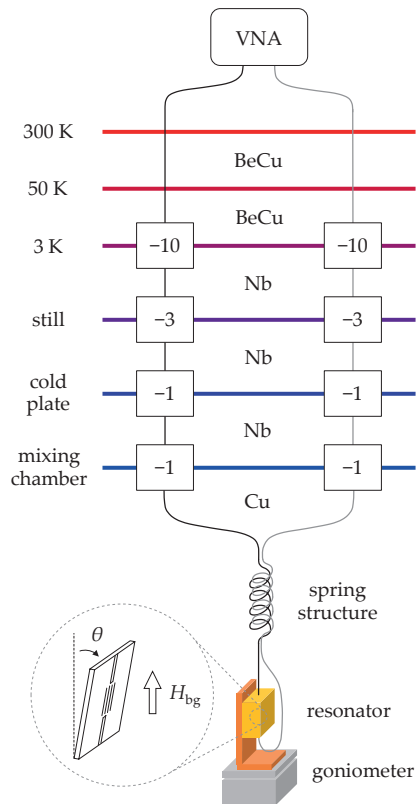


FIG. 3. Cabling and resonator configuration in the dilution refrigerator. Coaxial compositions are shown between stages. Numbers in boxes indicate attenuation. A nonmagnetic chip resistor (not shown) is attached on the backside of the L-shaped bracket to apply heat pulses to the resonator. The inset shows how a perpendicular field is applied by tilting.

maximum of the transmission coefficient. In Eq. (16), the second term is a complex background due to the direct coupling between the input and output ports through radiation.⁵⁸ The fitting parameters are $S_{21,\text{max}}$, f_{res} , Q_{load} , A , and ϕ .

The external quality factor Q_{ex} was obtained using the formula $Q_{\text{load}} = Q_{\text{ex}} 10^{-\text{IL}/20}$, where IL is the insertion loss in dB.⁵⁸ The insertion loss was estimated by subtracting the losses between the vector network analyzer and the package from $S_{21,\text{max}}$ in dB. The internal quality factor Q_{in} was obtained from the relation $Q_{\text{load}}^{-1} = Q_{\text{ex}}^{-1} + Q_{\text{in}}^{-1}$.

The circulating power P_{circ} was kept at about -20 dBm throughout the measurements. This value was high enough to suppress the loss due to two-level systems in the resonator dielectrics;⁵⁸ this value was also roughly 20 dB lower than the power where the quality factor is suppressed due to the nonlinearity. P_{circ} was estimated using $P_{\text{circ}} = \pi^{-1} P_{\text{inc}} Q_{\text{load}} 10^{-\text{IL}/20}$, where P_{inc} is the incident power on the input capacitor of the resonator.⁵⁸

Two cooling procedures were used: zero-field cooling (ZFC) and heat-pulsing (HP). For HP, a heat pulse (0.16

TABLE I. Properties of thin films. d is the film thickness. T_c is the critical temperature. Residual resistivity ratio (RRR) is defined by $R(300\text{ K})/R(T_c)$.

Wafer	Strip					Ground plane				
	d (nm)	Orient.	T_c (K)	ρ_n ($\mu\Omega\cdot\text{cm}$)	RRR	d (nm)	Orient.	T_c (K)	ρ_n ($\mu\Omega\cdot\text{cm}$)	RRR
A	50.5	(111)	9.30	2.9	6.3	48.4	(110), (111)	8.75	3.9	4.9
B	98.9	(111)	9.50	1.1	15.2	96.5	(110)	9.23	3.1	6.2
C	50	(110)	7.2	17	1.7	50	(110)			

TABLE II. Resonator information. The length of a strip is the same for all resonators, $5725\ \mu\text{m}$. f_0 and Q_0 are the resonance frequency and the loaded quality factors at $T_{\text{MC}} = 10\ \text{mK}$ without a magnetic field, where T_{MC} is the mixing chamber temperature. $Q_{0,\text{ex}}$ and $Q_{0,\text{in}}$ are the external and the internal quality factors in the same condition, respectively. Remark summarizes film quality, film thickness, and strip width of each resonator.

Res.	Wafer	W (μm)	S (μm)	G (μm)	Remark	f_0 (GHz)	Q_0	$Q_{0,\text{ex}}$	$Q_{0,\text{in}}$
1	A	60		300	clean and thin film, wide width	10.0078	3.34×10^4	6×10^4	8×10^4
2	A	15	75	400	clean and thin film, narrow width	10.0792	2.75×10^4	1×10^5	4×10^4
3	C	15	75	350	dirty and thin film, narrow width	10.0728	1.43×10^4	4×10^4	2×10^4
4	B	60		300	clean and thick film, wide width	10.0255	3.32×10^4	6×10^4	8×10^4

W for 5 s) is applied to completely suppress superconductivity. The resonator was then cooled in field. Note that a heat pulse was applied for each magnetic field value, unlike the ordinary field-cooling procedure in many studies.

To apply a perpendicular field, the resonator is tilted in a background field parallel to the microwave current H_{bg} by up to ± 3 deg using a goniometer (Attocube ANGt101), as shown in the inset of Fig. 3. H_{\perp} is obtained by $H_{\perp} = H_{\text{bg}} \sin\theta$. The precision at 100 mK is roughly ± 5 mdeg. Initial alignment was done at $\mu_0 H_{\text{bg}} = 0.7\ \text{T}$ after the HP procedure. The position of the goniometer that maximized f_{res} and Q_{load} was assumed to be $\theta = 0^\circ$. A spring structure is employed between the resonator and the mixing chamber to make the cables flexible.

For the rest of this paper, we will write the resonance frequency as f and the loaded quality factor as Q for simplicity.

IV. RESULTS AND ANALYSIS

A. Loss Parameters

In a magnetic field parallel to the film, the resonator performance is expected to be governed by quasiparticle generation due to the absence of the Lorentz force on vortices. Hence the loss parameters for quasiparticle generation can be obtained from the H_{\parallel} dependence of f and Q as shown in Fig. 4. The loss parameters for calculated curves are shown in Table III. The parameters

λ_0 , κ , and H_c were mostly determined by comparing the observed and expected f^{-2} . The expected f^{-2} was calculated using Eqs. (4)–(8) and $n_s(H_{\parallel})$ in Fig. 4(c). Here, $n_s(H_{\parallel})$ was obtained by solving the time-dependent GL equations. Then, $Q_{0,\text{fit}}$, β , and $\rho_{n,\text{fit}}$ were obtained from Q via similar procedures. (For details, see Sec. S3.)

The measured data and calculated curves agree well. In Table III, one can see that the dirtier film shows longer λ_0 , higher κ , and lower H_c , as expected.^{50,53} The values of λ_0 , κ , and H_c are reasonable, compared to previous reports.^{51,52,75,76} These results support that quasiparticle generation is the dominant loss mechanism in a parallel field and the loss can be understood quantitatively using the two-fluid model incorporated with the time-dependent GL equations.

Solving the GL equations for the actual geometry of resonators enabled us to determine the vortex penetration field parallel to the film $H_{\text{vp}}^{\parallel}$ of each resonator, indicated by vertical dashed lines in Fig. 4. Note that the H_{\parallel} dependence of n_s changes from quadratic to linear above $H_{\text{vp}}^{\parallel}$. This results in a change in the slope of $f^{-2}(H_{\parallel})$ and $Q(H_{\parallel})$ at 1.3 T (Res. 1 and 2) and 0.47 T (Res. 4).

In Table III, β varies between 0.4 and 2.2, and the film with higher d/λ_0 shows lower β . The microscopic description of these results using the standard theoretical expressions of the complex conductivity^{77–79} seems to be challenging,⁸⁰ because we cannot equate the order parameter, which is obtained from f^{-2} , to the energy gap in the presence of a perturbation that breaks the time-reversal symmetry.⁸¹ Although the energy gap suppression with field itself is understood well,^{81–83} we know

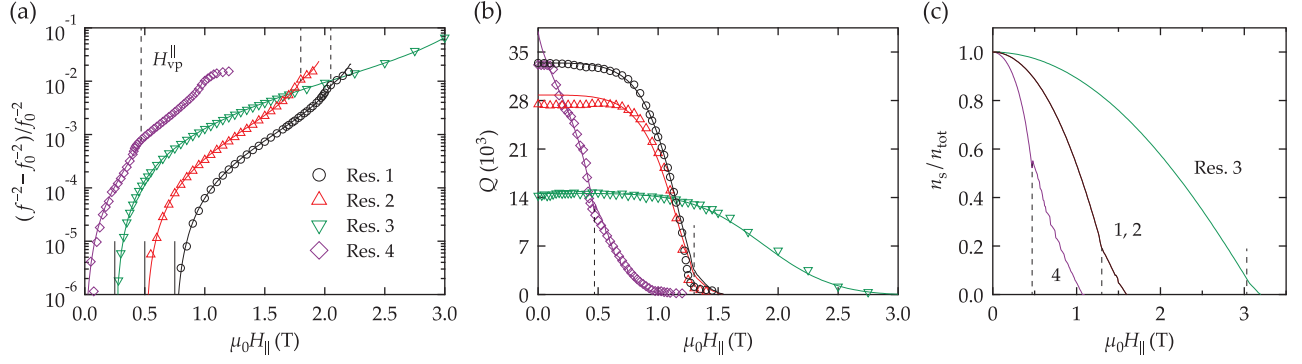


FIG. 4. (a,b) Parallel magnetic field H_{\parallel} dependence of f^{-2} and Q after ZFC. Solid lines are from calculations with parameters in Table III. In (a), f^{-2} data are shifted by 0.25 T steps for clarity. The offsets are indicated by vertical solid lines. (c) Parallel field dependence of n_s calculated by the GL equations. Vertical dashed lines indicate the vortex penetration field parallel to the film $H_{\text{vp}}^{\parallel}$ obtained from the solution of the GL equations. $H_{\text{vp}}^{\parallel}$ of Res. 3 is shown in (c) because its value is out of the experimental range. We also note that $H_{\text{vp}}^{\parallel}$ of Res. 1 and 2 are identical, even though they don't appear so in (a) due to the visual offset mentioned above. T_{MC} is less than 20 mK.

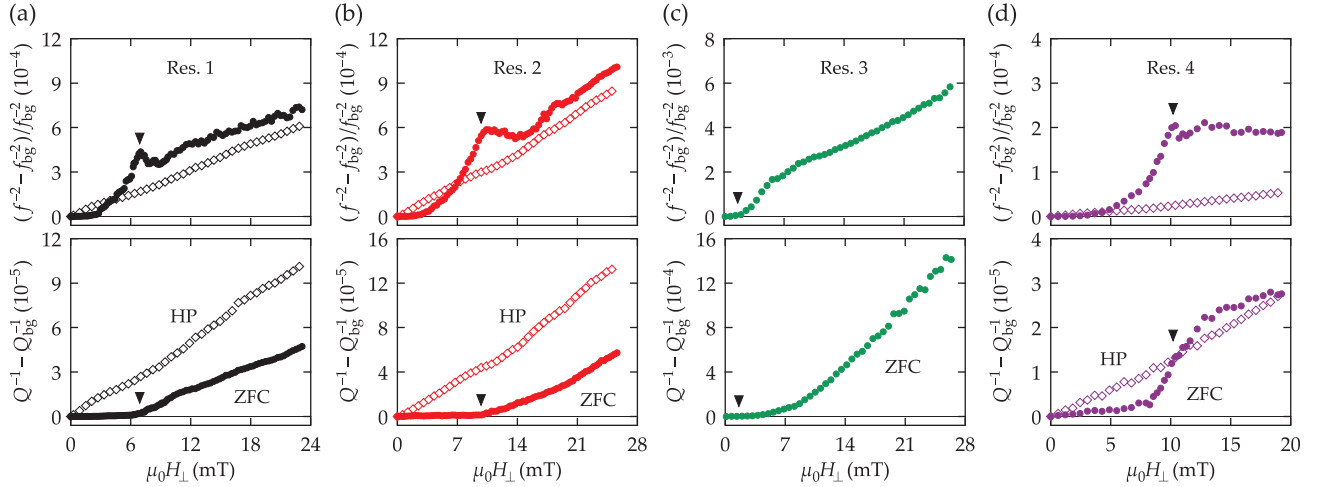


FIG. 5. Perpendicular magnetic field H_{\perp} dependence of f^{-2} and Q^{-1} . The subscript “bg” means that the quantity is measured with H_{bg} , but without tilting: $f_{\text{bg}} \equiv f(H_{\parallel} = H_{\text{bg}}, \theta = 0)$ and $Q_{\text{bg}} \equiv Q(H_{\text{bg}}, 0)$. $T_{\text{MC}} \approx 100$ mK and $\mu_0 H_{\text{bg}} = 0.35$ T. The cooling procedure for Res. 1, 2, and 4 is both ZFC and HP; for Res. 3, ZFC only. Note that the scales for f^{-2} and Q^{-1} are different from resonator to resonator. Arrows indicate the crossover field H_X , which is determined by plots of Q vs. f^{-2} (Fig. 7).

of no well-established expression that converts the order parameter to the energy gap for a type-II superconducting thin film in a parallel field. In our case, such an expression also needs to consider the spatial variation of the order parameter to account for vortices and the d/λ_0 dependence of β .

Figure 4(b) and Tables II and III show the trade-off between $Q_{0,\text{in}}$ and robustness against H_{\parallel} . The optimal condition for balancing these two factors can be written in terms of d/λ_0 . For $d/\lambda_0 < 1$ (Res. 3), Q does not change much by H_{\parallel} up to 1 T, but $Q_{0,\text{in}}$ is low; for $d/\lambda_0 > 1$ (Res. 4), $Q_{0,\text{in}}$ is high, but Q drops quickly in H_{\parallel} . Therefore, the resonator satisfying $d/\lambda_0 \approx 1$ (Res. 1 and 2) is the best choice for X-band ESR applications, which

require a magnetic field of 0.35 T.

Loss parameters associated with vortex motion are obtained by the HP procedure due to the homogeneous vortex distribution, as mentioned in Sec. II B 2. (For details, see Sec. S4.) Figure 5 shows the H_{\perp} dependence of f^{-2} and Q^{-1} after HP. For all resonators, f^{-2} and Q^{-1} vary linearly with the field and the intercept on the H_{\perp} axis is almost zero. These results indicate continuous occupation of vortices and a very low lower critical field.^{84,85}

Note that, in Table III, the better quality film shows a higher k_p . The reason is that, if the film is too dirty, the Bardeen-Cooper-Schrieffer coherence lengths deep within the grain and in the vicinity of the grain boundary are similar. This results in the pinning mechanism becoming

TABLE III. Loss parameters extracted from Figs. 4 and 5. Two characteristic fields, related to switching of the dominant loss mechanism, are also shown. $Q_{0,\text{fit}}$ is the zero-field Q determined by fitting; $\rho_{n,\text{fit}}$ is the residual resistivity obtained from fitting; H_{vp}^{\perp} is the vortex penetration field perpendicular to the film (see Sec. IV B); H_{X} is the crossover field (see Sec. IV C). Experimental conditions for each group of loss parameters are indicated in parentheses. For Res. 3, the ZFC data above 14 mT were used to obtain the loss parameters associated with vortex motion because of the absence of the HP data.

Res.	Quasiparticle generation (H_{\parallel} , ZFC)						Vortex motion (H_{\perp} , HP)			Char. field (H_{\perp} , ZFC)	
	λ_0 (nm)	κ	$\mu_0 H_c$ (mT)	$Q_{0,\text{fit}}$	β	$\rho_{n,\text{fit}}$ ($\mu\Omega\cdot\text{cm}$)	$\omega_p/2\pi$ (GHz)	η (N·s/m ²)	k_p (N/m ²)	$\mu_0 H_{\text{vp}}^{\perp}$ (mT)	$\mu_0 H_{\text{X}}$ (mT)
1	52	2.43	270	3.34×10^4	1.8	2.9	58	1.3×10^{-7}	4.8×10^4	6.9	6.9
2	52	2.43	270	2.88×10^4	1.8	2.9	62	1.2×10^{-7}	4.7×10^4	10.4	9.8
3	162	6.5	190	1.46×10^4	2.2	17	24	3.6×10^{-8}	5.9×10^3	5.5	2.2
4	43	1.80	250	3.80×10^4	0.4	0.6	20	1.9×10^{-6}	2.3×10^5	10.2	10.2

inefficient, although there may be more pinning sites.^{53,86} The better quality film has a higher η , as expected in Eq. (15).

B. Frequency Anomaly

1. Resonator 1

A key feature of Fig. 5 after ZFC is that an anomaly (peak/dip) appears in the f^{-2} data. This frequency anomaly is an indication of a partial release of the Meissner current along the edges, accompanied by vortex injection. This phenomenon is due to the strong repulsive interaction between the Meissner current and vortices.^{87–90} The field at which the frequency anomaly occurs is the vortex penetration field perpendicular to the film H_{vp}^{\perp} , i.e., the field at which the surface barrier is fully suppressed.

To support the above statement, we note that the H_{\perp} dependence of f^{-2} and Q^{-1} is different below and above H_{vp}^{\perp} . We start by exploring the dominant loss mechanism in both low and high field regimes of Res. 1 (Fig. 5(a)).

Below 7 mT, quasiparticle generation is the dominant contribution to f^{-2} and Q^{-1} , suggesting the existence of a large surface barrier. This is reflected in that (i) the H_{\perp} dependences of f^{-2} and Q^{-1} are qualitatively different from each other (see Sec. II B 2), and (ii) f^{-2} grows roughly quadratically.^{45,92–95} This is based on the approximate relation $(f^{-2} - f_0^{-2}) \propto -n_s$ (Eqs. (5), (6), and (8)) and n_s is suppressed approximately quadratically with a magnetic field (Fig. 4(c)).

Above 11 mT, vortex motion is the main contribution to microwave loss. Moreover, our results imply that a significant number of vortices are pinned near the center of the strip compared to the Bean-type model, even at the early stage of vortex penetration. The number of vortices increases linearly with H_{\perp} if the vortices accumulate near the center of the strip.⁷¹ Since the microwave current density near the center is roughly homogeneous and

much lower than at the edges (Fig. S1 in Sec. S2), the resulting f^{-2} and Q^{-1} are expected to be linear functions of H_{\perp} , and their slope should be less than that of the corresponding HP data (see Eqs. (1) and (13)).⁴⁰ These expectations are consistent with our results. In addition, the existence of a large surface barrier indicates that the critical current density associated with vortex pinning is significantly lower than the depairing current density. Hence, the vortex distribution is expected to deviate from the Bean-type model, which is valid when the critical current density is comparable to the depairing current density (Sec. II B 2).

From the discussions so far, we see that the dominant loss mechanism switches from quasiparticle generation to vortex motion around the field where the frequency anomaly occurs. To show how the suppression of the surface barrier and the switching of the dominant loss mechanism yield this frequency anomaly, we solved the time-dependent GL equations for a slab geometry with infinite thickness and length (y and z axes in the inset of Fig. 6(a)) in a magnetic field. (For details on the simulation conditions, see Sec. S1.) We use this geometry because the only difference between an infinite slab and a thin film is the strength of the interaction between the Meissner current and vortices. For a thin film, the interactions are stronger because the Meissner current and vortices interact mostly via stray magnetic fields (long-range interaction), while for a slab the interactions are exponential screening (short-range);^{89–91} the essential physics will remain intact.

Figure 6(a) shows how n_s decreases with a magnetic field. The jump at the magnetic field $H \approx 0.93H_c$ indicates vortex penetration. To obtain the quasiparticle contribution to f^{-2} , a weighting function $J_z^2(x)$ corresponding to the microwave current density distribution is needed. Since the geometry in (a) is neither a resonator nor a transmission line, $J_z^2(x)$ cannot be determined via the procedure described in Sec. S2. Here, we used a simple stepwise function as $J_z^2(x)$ (the inset of Fig. 6(b)). This weighting function maximizes contri-

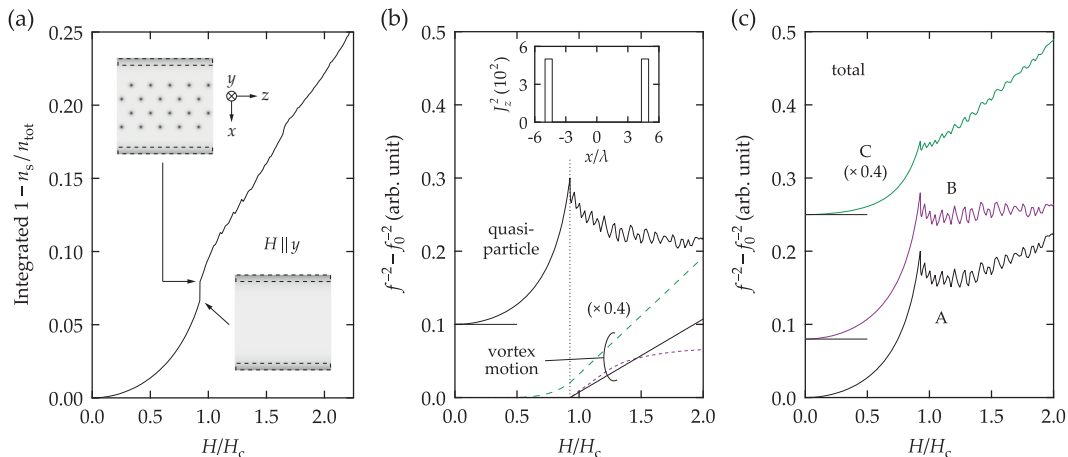


FIG. 6. Simulation of f^{-2} field dependence. (a) $1 - n_s/n_{\text{tot}}$, integrated over the geometry as a function of H . The insets show the normalized $|\psi(x, y)|$ before and after vortex penetration; darker is lower $|\psi(x, y)|$. Dashed rectangles are regions where the microwave current density is high. (b) f^{-2} from quasiparticle generation and vortex motion. The quasiparticle contribution is obtained from integration of $|\psi(x, y)|^{-2}$ with the weighting function $J_z^2(x)$. For the vortex motion contribution, curves imitating Q^{-1} in Fig. 5 are used. The dotted line indicates the vortex penetration field. The inset shows $J_z^2(x)$: $J_z^2 = 500$ from $x = \pm 4.3\lambda$ to $\pm W/2$ and $J_z^2 = 1$ for others. (c) Total f^{-2} , which is a summation of the contributions of quasiparticle generation and vortex motion in (b). The green lines in (b,c) are scaled with a factor of 0.4. Some data are shifted for clarity. The resonator-simulation correspondence is (Res. 1 and 2, A), (Res. 3, C), and (Res. 4, B).

butions from the region within roughly λ of the edges (shown by dashed lines in the insets of Fig. 6(a)), and the ratio between the values at the edge and the center is similar to that of our resonators. (See Sec. S2 for the ratio of $|J_z|^2$ between the edge and the center of the strips.) The result is shown in Fig. 6(b). f^{-2} shows a peak at the vortex penetration field, indicating that the number of quasiparticles near the edges are reduced, i.e., the Meissner current is partly released, while the total number of quasiparticles (including vortex cores) of the entire sample increases.

The vortex motion contribution is also shown in Fig. 6(b). As the width of the geometry for the simulation is much more confined than for the real strips and it does not have any pinning sites, curves imitating Q^{-1} in Fig. 5 are used as the vortex motion contribution. The total f^{-2} in Fig. 6(c) can be obtained by adding these vortex motion contributions to the quasiparticle contribution. The resulting curve A is quite similar to f^{-2} of Res. 1 (Fig. 5(a)).

The oscillatory behavior in Fig. 6(b,c) after vortex penetration is due to oscillation of the Meissner current during the subsequent injection of vortices; hence it can be understood as small variations of the frequency anomaly. These oscillations were experimentally observed as shown in Fig. 5 above H_{vp}^{\perp} .

Taken together, the inhomogeneous microwave current density distribution enables us to see the partial release of the Meissner current, which has previously only been observed in mesoscopic systems.^{87,88}

2. Other Resonators

The frequency anomaly of Res. 2 appears at a higher field (Fig. 5(b)). The reason is that, if the strip is narrower, less field accumulates at the edges. H_{vp}^{\perp} is expected to be proportional to $1/\sqrt{W}$,^{54,55} suggesting that H_{vp}^{\perp} of Res. 2 would be twice as high as that of Res. 1. The actual value is somewhat less (Table III), likely due to edge imperfections. Here, the field accumulation due to the multi-strip geometry is expected to be small because the distance between the strips is five times larger than the strip width.⁷²

The frequency anomaly of Res. 3 (Fig. 5(c)) is weak compared to others. This is due to low η and ω_p (Table III), resulting in a large contribution from vortex motion. The curve C in Fig. 6(c) shows such a case.

For Res. 4 (Fig. 5(d)), f^{-2} does not change significantly between 10 and 20 mT. This reflects that the vortex motion contribution is weaker than other resonators (Res. 4 has the highest η and the lowest ω_p) and the vortex distribution is close to the Bean-type model as a consequence of the stronger pinning as mentioned in Sec. IIB2. Since the microwave current density is high near the edge, the initial change in f^{-2} due to the vortex injection is large; as the field increases, the slope of f^{-2} decreases.⁴¹ This is represented by the curve B in Fig. 6(c).

By comparing Res. 2 and 3, we can study how H_{vp}^{\perp} is affected by the film quality. For the geometries of our resonators, the depairing current density scales with $1/\Lambda$,⁹⁶ while the Meissner current density scales with $1/\sqrt{\Lambda}$,⁵⁴ where Λ is the screening length given by

$2\lambda \coth(d/\lambda)$.^{97–99} Hence, the Meissner current density of the film with longer Λ meets the depairing current density earlier, i.e., the surface barrier is fully suppressed at a lower field. Our results are consistent with this: Res. 3, whose Λ is nearly an order of magnitude longer than that of Res. 2, shows low H_{vp}^{\perp} compared to that of Res. 2.

Increasing d also enhances H_{vp}^{\perp} , because the Meissner current density is roughly proportional to $1/d$ for thin films if Λ remains similar.⁵⁴ This is why Res. 4 shows higher H_{vp}^{\perp} than that of Res. 1. The film thickness, however, cannot be arbitrarily thick, because it needs to satisfy $d \approx \lambda_0$ (see Sec. IV A).

C. Q vs. f^{-2} Plot

We have discussed the dominant loss mechanism for H_{\parallel} and H_{\perp} with two cooling procedures. In general, however, identifying the dominant loss mechanism is not straightforward.

Figure 7(a,b) shows the H_{\perp} dependence of f^{-2} and Q^{-1} in various H_{bg} . The behavior of f^{-2} is qualitatively similar regardless of H_{bg} . One exception is the shift of the frequency anomaly to a lower H_{\perp} for a large H_{bg} , which is likely due to the elongation of λ by H_{bg} . However, the behavior of Q^{-1} at high H_{bg} is different, especially at $\gtrsim 1$ T: Q^{-1} increases significantly before the frequency anomaly. Note that Res. 3 and 4 in Fig. 5(c,d) also show a similar behavior.

A more informative way of displaying the data is to plot Q vs. f^{-2} , because each loss mechanism has its own characteristic relationship between the real and the imaginary parts of the complex resistivity. Figure 7(c–f) shows this and provides a clean indication of the dominant loss mechanism. In magnetic fields, where Q follows the parallel field data (gray line), the loss is dominated by quasiparticle generation; in fields, where Q is below the gray line, the loss is dominated by vortex motion. We identify the crossover fields H_{X} , where the dominant loss mechanism switches from quasiparticle generation to vortex motion, as the field where Q starts to deviate from the gray line. The arrows in Fig. 5 are obtained through this process.

V. CONCLUSION

In this work, we have developed an approach to characterizing the magnetic field dependent microwave losses in planar superconducting resonators. The parameters used to model the complex resistivity were obtained as the loss parameters (Table III) by comparing the experimentally determined f and Q as a function of magnetic field to calculated f and Q .

We found that quasiparticle generation is the dominant loss mechanism for parallel magnetic fields. For perpendicular magnetic fields, the dominant loss mechanism depends on the cooling procedure. After HP, vor-

tex motion is the dominant loss mechanism, while the dominating loss mechanism switches from quasiparticle generation to vortex motion after ZFC. For an arbitrary magnetic field direction and cooling history, the dominant loss mechanism can be readily identified from a plot of Q vs. f^{-2} .

A frequency anomaly was observed and interpreted as partial release of the Meissner current at the vortex penetration field. Simulations showed that the time-dependent GL equations and inhomogeneous microwave current density distribution provide an explanation of this frequency anomaly. This suggests that the interaction between vortices and the Meissner current near the edges is crucial for understanding the magnetic field dependence of the resonator properties.

We list three conditions that a planar resonator needs to satisfy for X-band ESR of thin films: (i) a high quality factor in a DC magnetic field of about 0.35 T, (ii) a highly homogeneous microwave magnetic field, and (iii) critical coupling to the external circuit.

Regarding condition (i), we have found that a niobium microstrip resonator satisfying $d \approx \lambda_0$ is a suitable choice: it gives reasonably high $Q_{0,\text{in}}$, while the quasiparticle loss induced by H_{\parallel} is low enough at 0.35 T. Improving the film quality is beneficial for reducing the loss induced by quasiparticle generation (via shorter λ , see Sec. II B 1) and vortex motion (via higher η and H_{vp}^{\perp}). Narrowing the strip width enhances H_{vp}^{\perp} , hence decreasing the number of vortices. Most importantly, a resonator has to be aligned precisely parallel to the magnetic field to minimize both the number of vortices and their motion. In this respect, we believe microstrip resonators are advantageous over coplanar waveguide resonators because there is no field accumulation between the strip and the ground plane, making them more robust against misalignment with respect to the perpendicular field.

Microstrip resonators are also advantageous for condition (ii). For microstrip resonators, a highly homogeneous microwave field is easily achievable by employing a multi-strip design, whereas applying the multi-strip design in coplanar waveguide or lumped element resonators does not seem to be straightforward.

As for condition (iii), critically coupled resonators can be made based on our results, especially the results shown in Tables II and III.

SUPPLEMENTARY MATERIALS

See the supplementary materials for details regarding solving the GL equations (Sec. S1), simulating the microwave current density distribution and the stored electromagnetic energy (Sec. S2), extracting the loss parameters (Secs. S3 and S4), and the film growth and characterization (Sec. S5).

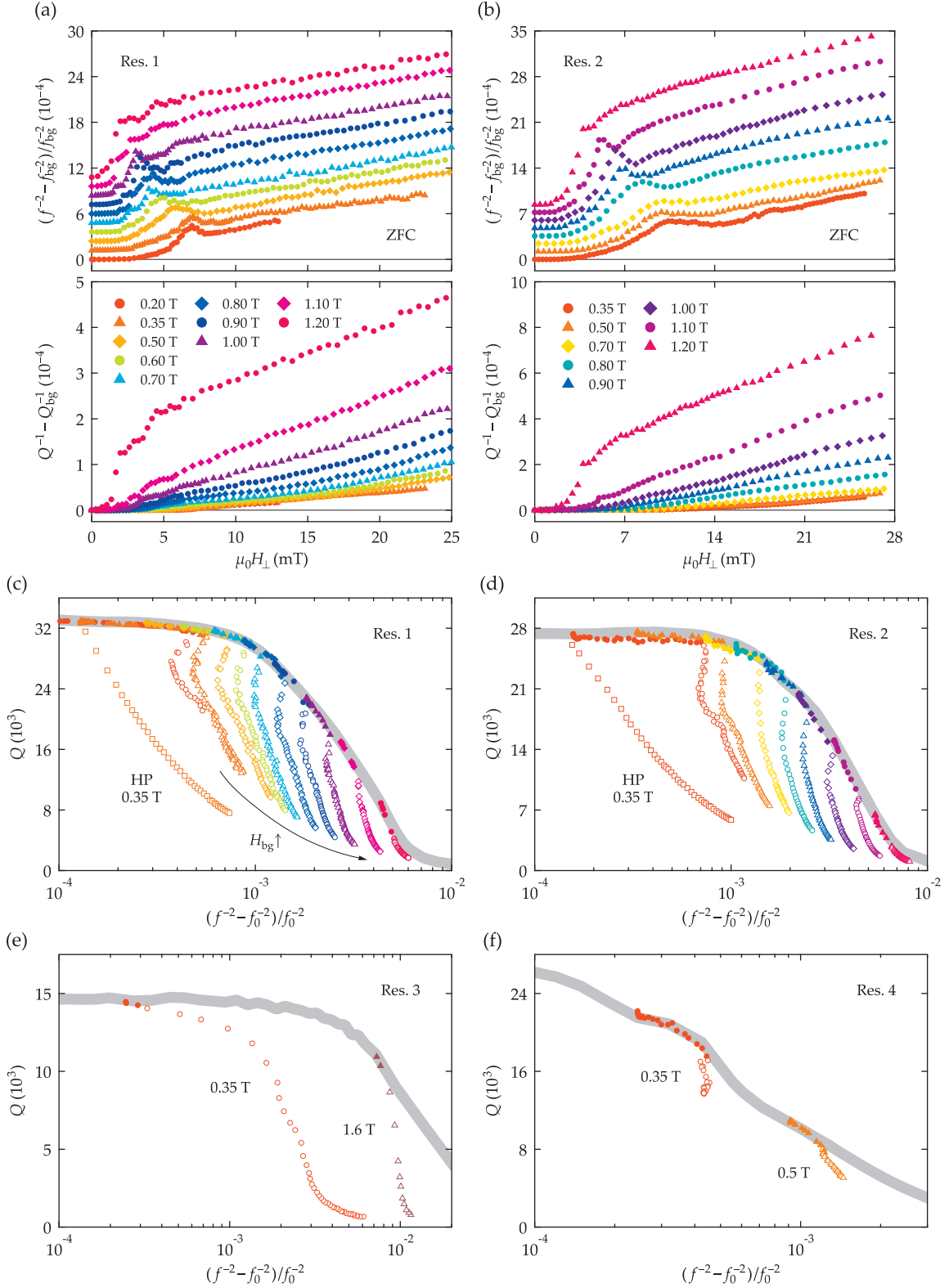


FIG. 7. (a,b) Perpendicular field dependence of f^{-2} and Q^{-1} in various H_{bg} for Res. 1 and 2 at $T_{MC} \approx 100$ mK. (c-f) Plots of Q vs. f^{-2} for Res. 1–4. In (c,d), the symbols and colors correspond to the same H_{bg} values as in the legend from (a,b). The gray line is the parallel field data shown in Fig. 4. All data are the ZFC data, except squares in (c,d) are the HP data with $\mu_0 H_{bg} = 0.35$ T. Solid symbols are the data whose loss is dominated by quasiparticle generation; empty symbols, dominated by vortex motion. In (a,b), f^{-2} data are shifted by 1.2×10^{-4} steps for clarity.

ACKNOWLEDGMENTS

S.K. thanks to A. Mitrovic, D. Carkner, Y. Ge for technical help, T. Matsushita, V. G. Kogan, G. P. Mikitik, E. Zeldov, R. Willa, T. W. Borneman for fruitful discussions, and the reviewers for helpful suggestions. This work is supported by the Canada First Research Excellence Fund, Canada Excellence Research Chairs (grant No. 215284), Natural Sciences and Engineering Research Council of Canada (grant Nos. RGPIN-418579 and RGPIN-04178), and Province of Ontario. The University of Waterloo's Quantum NanoFab was used for this work. This infrastructure is supported by the Canada Foundation for Innovation, the Ontario Ministry of Research & Innovation, Industry Canada, and Mike & Ophelia Lazaridis.

- ¹J. Zmuidzinas, *Superconducting Microresonators: Physics and Applications*, Annu. Rev. Condens. Matter Phys. **3**, 169 (2012).
- ²M. J. Lancaster, *Passive Microwave Device Applications of High-Temperature Superconductors* (Cambridge University Press, 1997).
- ³M. Hein, *High-Temperature-Superconductor Thin Films at Microwave Frequencies* (Springer, 1999).
- ⁴S. Haroche and J.-M. Raimond, *Exploring the Quantum: Atoms, Cavities, and Photons* (Oxford University Press, 2013).
- ⁵R. J. Schoelkopf and S. M. Girvin, *Wiring up Quantum Systems*, Nature **451**, 664 (2008).
- ⁶J. Clarke and F. K. Wilhelm, *Superconducting Quantum Bits*, Nature **453**, 1031 (2008).
- ⁷X. Gu, A. F. Kockum, A. Miranowicz, Y. X. Liu, and F. Nori, *Microwave Photonics with Superconducting Quantum Circuits*, Phys. Rep. **718-719**, 1 (2017).
- ⁸M. Wallquist, K. Hammerer, P. Rabl, M. Lukin, and P. Zoller, *Hybrid Quantum Devices and Quantum Engineering*, Phys. Scr. **T137**, 014001 (2009).
- ⁹M. Poot and H. S. J. van der Zant, *Mechanical Systems in the Quantum Regime*, Phys. Rep. **511**, 273 (2012).
- ¹⁰A. A. Houck, H. E. Türeci, and J. Koch, *On-Chip Quantum Simulation with Superconducting Circuits*, Nat. Phys. **8**, 292 (2012).
- ¹¹N. Daniilidis and H. Häffner, *Quantum Interfaces Between Atomic and Solid-State Systems*, Annu. Rev. Condens. Matter Phys. **4**, 83 (2013).
- ¹²M. Aspelmeyer, T. J. Kippenberg, and F. Marquardt, *Cavity Optomechanics*, Rev. Mod. Phys. **86**, 1391 (2014).
- ¹³J. J. L. Morton and B. W. Lovett, *Hybrid Solid-State Qubits: The Powerful Role of Electron Spins*, Annu. Rev. Condens. Matter Phys. **2**, 189 (2011).
- ¹⁴Z.-L. Xiang, S. Ashhab, J. Q. You, and F. Nori, *Hybrid Quantum Circuits: Superconducting Circuits Interacting with Other Quantum Systems*, Rev. Mod. Phys. **85**, 623 (2013).
- ¹⁵G. Kurizki, P. Bertet, Y. Kubo, K. Mølmer, D. Petrosyan, P. Rabl, and J. Schmiedmayer, *Quantum Technologies with Hybrid Systems*, Proc. Natl. Acad. Sci. U.S.A. **112**, 3866 (2015).
- ¹⁶A. Ghirri, A. Candini, and M. Affronte, *Molecular Spins in the Context of Quantum Technologies*, Magnetochemistry **2017**, 3, 12 (2017).
- ¹⁷M. U. Staudt, I.-C. Hoi, P. Krantz, M. Sandberg, M. Simoen, P. Bushev, N. Sangouard, M. Afzelius, V. S. Shumeiko, G. Johansson, P. Delsing, and C. M. Wilson, *Coupling of an Erbium Spin Ensemble to a Superconducting Resonator*, J. Phys. B: At. Mol. Opt. Phys. **45**, 124019 (2012).
- ¹⁸O. W. B. Benningshof, H. R. Mohebbi, I. A. J. Taminau, G. X. Miao, and D. G. Cory, *Superconducting Microstrip Resonator for Pulsed ESR of Thin Films*, J. Magn. Reson. **230**, 84 (2013).
- ¹⁹H. Malissa, D. I. Schuster, A. M. Tyryshkin, A. A. Houck, and S. A. Lyon, *Superconducting Coplanar Waveguide Resonators for Low Temperature Pulsed Electron Spin Resonance Spectroscopy*, Rev. Sci. Instr. **84**, 025116 (2013).
- ²⁰S. Probst, H. Rotzinger, S. Wünsch, P. Jung, M. Jerger, M. Siegel, A. V. Ustinov, and P. A. Bushev, *Anisotropic Rare-Earth Spin Ensemble Strongly Coupled to a Superconducting Resonator*, Phys. Rev. Lett. **110**, 157001 (2013).
- ²¹H. Huebl, C. W. Zollitsch, J. Lotze, F. Hocke, M. Greifenstein, A. Marx, R. Gross, and S. T. B. Goennenwein, *High Cooperativity in Coupled Microwave Resonator Ferrimagnetic Insulator Hybrids*, Phys. Rev. Lett. **111**, 127003 (2013).
- ²²A. J. Sigillito, H. Malissa, A. M. Tyryshkin, H. Riemann, N. V. Abrosimov, P. Becker, H.-J. Pohl, M. L. W. Thewalt, K. M. Itoh, J. J. L. Morton, A. A. Houck, D. I. Schuster, and S. A. Lyon, *Fast, Low-Power Manipulation of Spin Ensembles in Superconducting Microresonators*, Appl. Phys. Lett. **104**, 222407 (2014).
- ²³C. Grezes, B. Julsgaard, Y. Kubo, M. Stern, T. Umeda, J. Isoya, H. Sumiya, H. Abe, S. Onoda, T. Ohshima, V. Jacques, J. Esteve, D. Vion, D. Esteve, K. Mølmer, and P. Bertet, *Multimode Storage and Retrieval of Microwave Fields in a Spin Ensemble*, Phys. Rev. X **4**, 021049 (2014).
- ²⁴A. Tkalcic, S. Probst, D. Rieger, H. Rotzinger, S. Wünsch, N. Kukharchyk, A. D. Wieck, M. Siegel, A. V. Ustinov, and P. Bushev, *Strong Coupling of an Er³⁺-Doped YAlO₃ Crystal to a Superconducting Resonator*, Phys. Rev. B **90**, 075112 (2014).
- ²⁵S. Putz, D. O. Krimer, R. Amsüss, A. Valookaran, T. Nöbauer, J. Schmiedmayer, S. Rotter, and J. Majer, *Protecting a Spin Ensemble Against Decoherence in the Strong-Coupling Regime of Cavity QED*, Nature Phys. **10**, 720 (2014).
- ²⁶I. Wisby, S. E. de Graaf, R. Gwilliam, A. Adamyan, S. E. Kubatkin, P. J. Meeson, A. Ya. Tzalenchuk, and T. Lindström, *Coupling of a Locally Implanted Rare-Earth Ion Ensemble to a Superconducting Microresonator*, Appl. Phys. Lett. **105**, 102601 (2014).
- ²⁷A. Ghirri, C. Bonizzoni, D. Gerace, S. Sanna, A. Cassinese, and M. Affronte, *YBa₂Cu₃O₇ Microwave Resonators for Strong Collective Coupling with Spin Ensembles*, Appl. Phys. Lett. **106**, 184101 (2015).
- ²⁸C. Grezes, B. Julsgaard, Y. Kubo, W. L. Ma, M. Stern, A. Bienfait, K. Nakamura, J. Isoya, S. Onoda, T. Ohshima, V. Jacques, D. Vion, D. Esteve, R. B. Liu, K. Mølmer, and P. Bertet, *Storage and Retrieval of Microwave Fields at the Single-Photon Level in a Spin Ensemble*, Phys. Rev. A **92**, 020301(R) (2015).
- ²⁹C. W. Zollitsch, K. Mueller, D. P. Franke, S. T. B. Goennenwein, M. S. Brandt, R. Gross, and H. Huebl, *High Cooperativity Coupling between a Phosphorus Donor Spin Ensemble and a Superconducting Microwave Resonator*, Appl. Phys. Lett. **107**, 142105 (2015).
- ³⁰A. Bienfait, J. J. Pla, Y. Kubo, M. Stern, X. Zhou, C. C. Lo, C. D. Weis, T. Schenkel, M. L. W. Thewalt, D. Vion, D. Esteve, B. Julsgaard, K. Mølmer, J. J. L. Morton, and P. Bertet, *Reaching the Quantum Limit of Sensitivity in Electron Spin Resonance*, Nat. Nanotechnol. **11**, 253 (2016).
- ³¹A. Bienfait, J. J. Pla, Y. Kubo, X. Zhou, M. Stern, C. C. Lo, C. D. Weis, T. Schenkel, D. Vion, D. Esteve, J. J. L. Morton, and P. Bertet, *Controlling Spin Relaxation with a Cavity*, Nature **531**, 74 (2016).
- ³²C. Bonizzoni, A. Ghirri, K. Bader, J. van Slageren, M. Perfetti, L. Sorace, Y. Lan, O. Fuhr, M. Ruben, and M. Affronte, *Coupling Molecular Spin Centers to Microwave Planar Resonators: towards Integration of Molecular Qubits in Quantum Circuits*, Dalton Trans. **45**, 16596 (2016).
- ³³I. S. Wisby, S. E. de Graaf, R. Gwilliam, A. Adamyan, S. E. Kubatkin, P. J. Meeson, A. Ya. Tzalenchuk, and T. Lindström, *Angle-Dependent Microresonator ESR Characterization of Locally Doped Gd³⁺:Al₂O₃*, Phys. Rev. Applied **6**, 024021 (2016).

- ³⁴C. Eichler, A. J. Sigillito, S. A. Lyon, and J. R. Petta, *Electron Spin Resonance at the Level of 10^4 Spins Using Low Impedance Superconducting Resonators*, Phys. Rev. Lett. **118**, 037701 (2017).
- ³⁵T. Astner, S. Nevlacsil, N. Peterschofsky, A. Angerer, S. Rotter, S. Putz, J. Schmiedmayer, and J. Majer, *Coherent Coupling of Remote Spin Ensembles via a Cavity Bus*, Phys. Rev. Lett. **118**, 140502 (2017).
- ³⁶H. R. Mohebbi, O. W. B. Benningshof, I. A. J. Taminiou, G. X. Miao, and D. G. Cory, *Composite Arrays of Superconducting Microstrip Line Resonators*, J. Appl. Phys. **115**, 094502 (2014).
- ³⁷L. Frunzio, A. Wallraff, D. Schuster, J. Majer, and R. Schoelkopf, *Fabrication and Characterization of Superconducting Circuit QED Devices for Quantum Computation*, IEEE Trans. Appl. Supercond. **15**, 860 (2005).
- ³⁸C. Song, M. P. DeFeo, K. Yu, and B. L. T. Plourde, *Reducing Microwave Loss in Superconducting Resonators due to Trapped Vortices*, Appl. Phys. Lett. **95**, 232501 (2009).
- ³⁹D. Bothner, T. Gaber, M. Kemmler, D. Koelle, and R. Kleiner, *Improving the Performance of Superconducting Microwave Resonators in Magnetic Fields*, Appl. Phys. Lett. **98**, 102504 (2011).
- ⁴⁰D. Bothner, C. Clauss, E. Koroknay, M. Kemmler, T. Gaber, M. Jetter, M. Scheffler, P. Michler, M. Dressel, D. Koelle, and R. Kleiner, *Reducing Vortex Losses in Superconducting Microwave Resonators with Microsphere Patterned Antidot Arrays*, Appl. Phys. Lett. **100**, 012601 (2012).
- ⁴¹D. Bothner, T. Gaber, M. Kemmler, D. Koelle, R. Kleiner, S. Wunsch, and M. Siegel, *Magnetic Hysteresis Effects in Superconducting Coplanar Microwave Resonators*, Phys. Rev. B **86**, 014517 (2012).
- ⁴²S. E. de Graaf, A. V. Danilov, A. Adamyan, T. Bauch, and S. E. Kubatkin, *Magnetic Field Resilient Superconducting Fractal Resonators for Coupling to Free Spins*, J. Appl. Phys. **112**, 123905 (2012).
- ⁴³S. E. de Graaf, D. Davidovikj, A. Adamyan, S. E. Kubatkin, and A. V. Danilov, *Galvanically Split Superconducting Microwave Resonators for Introducing Internal Voltage Bias*, Appl. Phys. Lett. **104**, 052601 (2014).
- ⁴⁴V. Singh, B. H. Schneider, S. J. Bosman, E. P. J. Merckx, and G. A. Steele, *Molybdenum-Rhenium Alloy Based High-Q Superconducting Microwave Resonators*, Appl. Phys. Lett. **105**, 222601 (2014).
- ⁴⁵N. Samkharadze, A. Bruno, P. Scarlino, G. Zheng, D. P. DiVincenzo, L. DiCarlo, and L. M. K. Vandersypen, *High-Kinetic-Inductance Superconducting Nanowire Resonators for Circuit QED in a Magnetic Field*, Phys. Rev. Applied **5**, 044004 (2016).
- ⁴⁶Y.-C. Tang, H. Zhang, S. Kwon, H. R. Mohebbi, D. G. Cory, L.-C. Peng, L. Gu, H.-Z. Guo, K.-J. Jinn and G.-X. Miao, *Superconducting Resonators Based on TiN/Tapering/NbN/Tapering/TiN Heterostructures*, Adv. Eng. Mater. **18**, 1816 (2016).
- ⁴⁷N. G. Ebensperger, M. Thiemann, M. Dressel, and M. Scheffler, *Superconducting Pb Stripline Resonators in Parallel Magnetic Field and Their Application for Microwave Spectroscopy*, Supercond. Sci. Technol. **29**, 115004 (2016).
- ⁴⁸Y.-C. Tang, S. Kwon, H. R. Mohebbi, D. G. Cory, and G.-X. Miao, *Phonon Engineering in Proximity Enhanced Superconductor Heterostructures*, Sci. Rep. **7**, 4282 (2017).
- ⁴⁹D. Bothner, D. Wiedmaier, B. Ferdinand, R. Kleiner, and D. Koelle, *Improving Superconducting Resonators in Magnetic Fields by Reduced Field Focussing and Engineered Flux Screening*, Phys. Rev. Applied **8**, 034025 (2017).
- ⁵⁰M. Tinkham, *Introduction to Superconductivity*, 2nd ed. (McGraw-Hill, 1996).
- ⁵¹A. I. Gubin, K. S. Il'in, S. A. Vitusevich, M. Siegel, and N. Klein, *Dependence of Magnetic Penetration Depth on the Thickness of Superconducting Nb Thin Films*, Phys. Rev. B **72**, 064503 (2005).
- ⁵²T. R. Lemberger, I. Hetel, J. W. Knepper, and F. Y. Yang, *Penetration Depth Study of Very Thin Superconducting Nb Films*, Phys. Rev. B **76**, 094515 (2007).
- ⁵³T. Matsushita, *Flux Pinning in Superconductors*, 2nd ed. (Springer, 2014).
- ⁵⁴A. V. Kuznetsov, D. V. Eremanko, and V. N. Trofimov, *Onset of Flux Penetration into a Thin Superconducting Film Strip*, Phys. Rev. B **59**, 1507 (1999).
- ⁵⁵E. H. Brandt, G. P. Mikitik, and E. Zeldov, *Two Regimes of Vortex Penetration into Platelet-Shaped Type-II Superconductors*, J. Exp. Theor. Phys., **117**, 439 (2013).
- ⁵⁶C. P. Bean and J. D. Livingston, *Surface Barrier in Type-II Superconductors*, Phys. Rev. Lett. **12**, 14 (1964).
- ⁵⁷M. Göppl, A. Fragner, M. Baur, R. Bianchetti, S. Filipp, J. M. Fink, P. J. Leek, G. Puebla, L. Steffen, and A. Wallraff, *Coplanar Waveguide Resonators for Circuit Quantum Electrodynamics*, J. Appl. Phys. **104**, 113904 (2008).
- ⁵⁸J. M. Sage, V. Bolkhovskiy, W. D. Oliver, B. Turek, and P. B. Welander, *Study of Loss in Superconducting Coplanar Waveguide Resonators*, J. Appl. Phys. **109**, 063915 (2011).
- ⁵⁹J. Goetz, F. Deppe, M. Haeberlein, F. Wulschner, C. W. Zollitsch, S. Meier, M. Fischer, P. Eder, E. Xie, K. G. Fedorov, E. P. Menzel, A. Marx, and R. Gross, *Loss Mechanisms in Superconducting Thin Film Microwave Resonators*, J. Appl. Phys. **119**, 015304 (2016).
- ⁶⁰M. W. Coffey and J. R. Clem, *Unified Theory of Effects of Vortex Pinning and Flux Creep upon the rf Surface Impedance of Type-II Superconductors*, Phys. Rev. Lett. **67**, 386 (1991).
- ⁶¹E. H. Brandt, *Penetration of Magnetic ac Fields into Type-II Superconductors*, Phys. Rev. Lett. **67**, 2219 (1991).
- ⁶²A. Dulčić and M. Požek, *Microwave Surface Impedance in the Mixed State of Type-II Superconductors*, Physica C **218**, 449 (1993).
- ⁶³N. Pompeo and E. Silva, *Reliable Determination of Vortex Parameters from Measurements of the Microwave Complex Resistivity*, Phys. Rev. B **78**, 094503 (2008).
- ⁶⁴E. Silva, N. Pompeo, S. Sarti, and C. Amabile, *Vortex State Microwave Response in Superconducting Cuprates and MgB₂*, in *Recent Developments in Superconductivity Research*, edited by B. P. Martins (Nova Science Publishers, New York, 2007).
- ⁶⁵N. B. Kopnin, *Theory of Nonequilibrium Superconductivity* (Oxford University Press, 2001).
- ⁶⁶C. Song, T. W. Heitmann, M. P. DeFeo, K. Yu, R. McDermott, M. Neeley, J. M. Martinis, and B. L. T. Plourde, *Microwave Response of Vortices in Superconducting Thin Films of Re and Al*, Phys. Rev. B **79**, 174512 (2009).
- ⁶⁷Th. Schuster, M. V. Indenbom, H. Kuhn, E. H. Brandt, and M. Konczykowski, *Flux Penetration and Overcritical Currents in Flat Superconductors with Irradiation-Enhanced Edge Pinning: Theory and Experiment*, Phys. Rev. Lett. **73**, 1424 (1994).
- ⁶⁸E. Zeldov, A. I. Larkin, V. B. Geshkenbein, M. Konczykowski, D. Majer, B. Khaykovich, V. M. Vinokur, and H. Shtrikman, *Geometrical Barriers in High-Temperature Superconductors*, Phys. Rev. Lett. **73**, 1428 (1994).
- ⁶⁹E. Zeldov, A. I. Larkin, M. Konczykowski, B. Khaykovich, D. Majer, V. B. Geshkenbein, and V. M. Vinokur, *Geometrical Barriers in Type-II Superconductors*, Physica C **235-240**, 2761 (1994).
- ⁷⁰Th. Schuster, H. Kuhn, E. H. Brandt, M. Indenbom, M. R. Koblischka, and M. Konczykowski, *Flux Motion in Thin Superconductors with Inhomogeneous Pinning*, Phys. Rev. B **50**, 16684 (1994).
- ⁷¹I. L. Maksimov and A. A. Elistratov, *Edge Barrier and Structure of the Critical State in Superconducting Thin Films*, JETP Lett. **61**, 208 (1995).
- ⁷²R. Willa, V. B. Geshkenbein, and G. Blatter, *Suppression of Geometric Barrier in Type-II Superconducting Strips*, Phys. Rev. B **89**, 104514 (2014).
- ⁷³E. H. Brandt and M. Indenbom, *Type-II-Superconductor Strip with Current in a Perpendicular Magnetic Field*, Phys. Rev. B

- 48, 12893 (1993).
- ⁷⁴E. Zeldov, J. R. Clem, M. McElkesh, and M. Darwin, *Magnetization and Transport Currents in Thin Superconducting Films*, Phys. Rev. B **49**, 9802 (1994).
- ⁷⁵C. C. Koch, J. O. Scarbrough, and D. M. Kroeger, *Effects of Interstitial Oxygen on the Superconductivity of Niobium*, Phys. Rev. B **9**, 888 (1974).
- ⁷⁶J. Halbritter, *Transport in Superconducting Niobium Films for Radio Frequency Applications*, J. Appl. Phys. **97**, 083904 (2005).
- ⁷⁷D. C. Mattis and J. Bardeen, *Theory of the Anomalous Skin Effect in Normal and Superconducting Metals*, Phys. Rev. **111**, 412 (1958).
- ⁷⁸W. Zimmermann, E. H. Brandt, M. Bauer, E. Seider, and L. Genzel, *Optical Conductivity of BCS Superconductors with Arbitrary Purity*, Physica C **183**, 99 (1991).
- ⁷⁹M. Dressel, *Electrodynamics of Metallic Superconductors*, Adv. Condens. Matter Phys. **2013**, 104379 (2013).
- ⁸⁰R. H. White and M. Tinkham, *Magnetic-Field Dependence of Microwave Absorption and Energy Gap in Superconducting Films*, Phys. Rev. **136**, A203 (1964).
- ⁸¹K. Maki, *Gapless Superconductivity*, in *Superconductivity*, edited by R. D. Parks (Marcel Dekker, New York, 1969), Vol. 2, p. 1035.
- ⁸²K. D. Usadel, *Generalized Diffusion Equation for Superconducting Alloys*, Phys. Rev. Lett. **25**, 507 (1970).
- ⁸³A. Anthore, H. Pothier, and D. Esteve, *Density of States in a Superconductor Carrying a Supercurrent*, Phys. Rev. Lett. **90**, 127001 (2003).
- ⁸⁴G. Stan, S. B. Field, and J. M. Martinis, *Critical Field for Complete Vortex Expulsion from Narrow Superconducting Strips*, Phys. Rev. Lett. **92**, 097003 (2004).
- ⁸⁵K. H. Kuit, J. R. Kirtley, W. van der Veur, C. G. Molenaar, F. J. G. Roesthuis, A. G. P. Troeman, J. R. Clem, H. Hilgenkamp, H. Rogalla, and J. Flokstra, *Vortex Trapping and Expulsion in Thin-Film $YBa_2Cu_3O_{7-\delta}$ Strips*, Phys. Rev. B **77**, 134504 (2008).
- ⁸⁶G. Zerweck, *On Pinning of Superconducting Flux Lines by Grain Boundaries*, J. Low Temp. Phys. **42**, 1 (1981).
- ⁸⁷A. K. Geim, S. V. Dubonos, I. V. Grigorieva, K. S. Novoselov, F. M. Peeters, and V. A. Schweigert, *Non-Quantized Penetration of Magnetic Field in the Vortex State of Superconductors*, Nature **407**, 55 (2000).
- ⁸⁸F. M. Peeters, V. A. Schweigert, and B.J. Baelus, *Fractional and Negative Flux Penetration in Mesoscopic Superconducting Disks*, Physica C **369**, 158 (2002).
- ⁸⁹A. L. Fetter, *Flux Penetration in a Thin Superconducting Disk*, Phys. Rev. B **22**, 1200 (1980).
- ⁹⁰V. G. Kogan, *Pearl's Vortex Near the Film Edge*, Phys. Rev. B **49**, 15874 (1994).
- ⁹¹J. Pearl, *Current Distribution in Superconducting Films Carrying Quantized Fluxoids*, Appl. Phys. Lett. **5**, 65 (1964).
- ⁹²Yu. V. Sharvin and V. F. Gantmakher, *Dependence of the Depth of Penetration of the Magnetic Field in a Superconductor on the Magnetic Field Strength*, Sov. Phys. JETP **12**, 866 (1961).
- ⁹³D. H. Douglass, Jr., *Magnetic Field Dependence of the Superconducting Penetration Depth in Thin Specimens*, Phys. Rev. **124**, 735 (1961).
- ⁹⁴S. Sridhar, D.-H. Wu, and W. Kennedy, *Temperature Dependence of Electrodynamical Properties of $YBa_2Cu_3O_y$ Crystals*, Phys. Rev. Lett. **63**, 1873 (1989).
- ⁹⁵J. E. Healey, T. Lindström, M. S. Colclough, C. M. Muirhead, and A. Ya. Tzalenchuk, *Magnetic Field Tuning of Coplanar Waveguide Resonators*, Appl. Phys. Lett. **93**, 043513 (2008).
- ⁹⁶J. R. Clem and K. K. Berggren, *Geometry-Dependent Critical Currents in Superconducting Nanocircuits*, Phys. Rev. B **84**, 174510 (2011).
- ⁹⁷N. Klein, H. Chaloupka, G. Müller, S. Orbach, H. Piel, B. Roas, L. Schultz, U. Klein, and M. Peiniger, *The Effective Microwave Surface Impedance of High T_c Thin Films*, J. Appl. Phys. **67**, 6940 (1990).
- ⁹⁸D. Yu. Irz, V. N. Ryzhov, and E. E. Tareyeva, *Vortex-Vortex Interaction in a Superconducting Film of Finite Thickness*, Phys. Lett. A **207**, 374 (1995).
- ⁹⁹J.-C. Wei and T.-J. Yang, *Current Distribution and Vortex-Vortex Interaction in a Superconducting Film of Finite Thickness*, Jpn. J. Appl. Phys. **35**, 5696 (1996).
- ¹⁰⁰A. Schmid, *A Time Dependent Ginzburg-Landau Equation and its Application to the Problem of Resistivity in the Mixed State*, Phys. kondens. Materie **5**, 302 (1966).
- ¹⁰¹W. D. Gropp, H. G. Kaper, G. K. Leaf, D. M. Levine, M. Palumbo, and V. M. Vinokur, *Numerical Simulation of Vortex Dynamics in Type-II Superconductors*, J. Comput. Phys. **123**, 254 (1996).
- ¹⁰²T. S. Alström, M. P. Sørensen, N. F. Pedersen, and S. Madsen, *Magnetic Flux Lines in Complex Geometry Type-II Superconductors Studied by the Time Dependent Ginzburg-Landau Equation*, Acta. Appl. Math. **115**, 63 (2011).
- ¹⁰³D. M. Sheen, S. M. Ali, D. E. Oates, R. S. Withers, and J. A. Kong, *Current Distribution, Resistance, and Inductance for Superconducting Strip Transmission Lines*, IEEE Trans. Appl. Supercond. **1**, 108 (1991).
- ¹⁰⁴W. H. Chang, *The Inductance of a Superconducting Strip Transmission Line*, J. Appl. Phys. **50**, 8129 (1979).
- ¹⁰⁵W. Kern, *The Evolution of Silicon Wafer Cleaning Technology*, J. Electrochem. Soc. **137**, 1887 (1990).
- ¹⁰⁶J. Wenner, R. Barends, R. C. Bialczak, Yu Chen, J. Kelly, E. Lucero, M. Mariantoni, A. Megrant, P. J. J. O'Malley, D. Sank, A. Vainsencher, H. Wang, T. C. White, Y. Yin, J. Zhao, A. N. Cleland, and J. M. Martinis, *Surface Loss Simulations of Superconducting Coplanar Waveguide Resonators*, Appl. Phys. Lett. **99**, 113513 (2011).
- ¹⁰⁷A. Megrant, C. Neill, R. Barends, B. Chiaro, Yu Chen, L. Feigl, J. Kelly, E. Lucero, M. Mariantoni, P. J. J. O'Malley, D. Sank, A. Vainsencher, J. Wenner, T. C. White, Y. Yin, J. Zhao, C. J. Palmström, J. M. Martinis, and A. N. Cleland, *Planar Superconducting Resonators with Internal Quality Factors above one Million*, Appl. Phys. Lett. **100**, 113510 (2012).
- ¹⁰⁸C.-B. Eom and J. M. Murduck, *Synthesis and Characterization of Superconducting Thin Films*, Thin Films **28**, 227 (2001).
- ¹⁰⁹T. Wagner, M. Lorenz, and M. Rühle, *Thermal Stability of Nb Thin Films on Sapphire*, J. Mater. Res. **11**, 1255 (1996).
- ¹¹⁰K. Mašek and V. Matolín, *RHEED Study of Nb Thin Film Growth on α - Al_2O_3 (0001) Substrate*, Thin Solid Films **317**, 183 (1998).
- ¹¹¹A. R. Wildes, J. Mayer, and K. Theis-Bröhl, *The Growth and Structure of Epitaxial Niobium on Sapphire*, Thin Solid Films **401**, 7 (2001).
- ¹¹²Keithley, *Low Level Measurements Handbook*, 7th ed. (2013).

Supplementary Materials

S1 Time-dependent Ginzburg–Landau Equations

The time-dependent Ginzburg–Landau (GL) equations are given by (in SI units)^{65,100,101}

$$-\frac{\hbar^2}{2m_s D} \left(\frac{\partial}{\partial t} + \frac{ie_s}{\hbar} \phi \right) \psi = \alpha \psi + \beta |\psi|^2 \psi + \frac{1}{2m_s} \left(\frac{\hbar}{i} \nabla - e_s \vec{A} \right)^2 \psi, \quad (\text{S1})$$

$$\frac{1}{\mu_0} \nabla \times \nabla \times \vec{A} = \frac{e_s \hbar}{2m_s i} (\psi^* \nabla \psi - \psi \nabla \psi^*) - \frac{e_s^2}{m_s} |\psi|^2 \vec{A} + \sigma_n \left(-\frac{\partial \vec{A}}{\partial t} - \nabla \phi \right), \quad (\text{S2})$$

where $\psi = \psi(x, y, z, t)$ is the complex order parameter; α and β are phenomenological parameters; D is the phenomenological diffusion coefficient; e_s and m_s are the charge and the mass of the superconducting electron, respectively; \vec{A} is the magnetic vector potential; ϕ is the electric potential; and σ_n is the inverse of the residual resistivity. The applied magnetic field \vec{H}_a is assumed uniform, $\nabla \times \vec{H}_a = 0$.

Boundary conditions at the surface of a superconducting sample are given by

$$\nabla \times \vec{A} = \mu_0 \vec{H}_a, \quad \vec{J}_s \cdot \vec{n} = 0, \quad \sigma_n \vec{E} \cdot \vec{n} = 0, \quad (\text{S3})$$

where J_s is the supercurrent density. The last two conditions ensure that no current passes through the surface. These conditions can also be written as

$$\left(\frac{\hbar}{i} \nabla \psi - e_s \vec{A} \psi \right) \cdot \vec{n} = 0, \quad \left(\frac{\partial \vec{A}}{\partial t} + \nabla \phi \right) \cdot \vec{n} = 0. \quad (\text{S4})$$

We transform the GL equations into dimensionless quantities by measuring length in units of the penetration depth λ ; time in units of the characteristic relaxation time $\tau \equiv \xi^2/D$, where ξ is the GL coherence length; fields in units of $\sqrt{2}H_c$, where H_c is the thermodynamic critical field; and order parameter in units of $\psi_0 \equiv \sqrt{|\alpha|/\beta}$. Then, Eqs. (S1) and (S2) become¹⁰¹

$$\left(\frac{\partial}{\partial t} + i\kappa\phi \right) \psi = - \left(\frac{i}{\kappa} \nabla + \vec{A} \right)^2 \psi + \psi - |\psi|^2 \psi, \quad (\text{S5})$$

$$\sigma_n \left(\frac{\partial \vec{A}}{\partial t} + \nabla \phi \right) = \frac{1}{2i\kappa} (\psi^* \nabla \psi - \psi \nabla \psi^*) - |\psi|^2 \vec{A} - \nabla \times \nabla \times \vec{A}, \quad (\text{S6})$$

where $\kappa \equiv \lambda/\xi$ is the GL parameter.

The time-dependent GL equations are invariant under the gauge transformation with a function $\chi(x, y, z, t)$:

$$\tilde{\psi} = \psi e^{i\kappa\chi}, \quad \tilde{\vec{A}} = \vec{A} + \nabla\chi, \quad \tilde{\phi} = \phi - \frac{\partial\chi}{\partial t}.$$

For convenience, we choose the zero-electric potential gauge, $\tilde{\phi} = 0$. Dropping tildes, Eqs. (S5) and (S6) are written as

$$\frac{\partial\psi}{\partial t} = - \left(\frac{i}{\kappa} \nabla + \vec{A} \right)^2 \psi + \psi - |\psi|^2 \psi, \quad (\text{S7})$$

$$\sigma_n \frac{\partial \vec{A}}{\partial t} = \frac{1}{2i\kappa} (\psi^* \nabla \psi - \psi \nabla \psi^*) - |\psi|^2 \vec{A} - \nabla \times \nabla \times \vec{A}. \quad (\text{S8})$$

The equations for the boundary conditions, Eqs. (S3) and (S4), become

$$\nabla \times \vec{A} - \mu_0 \vec{H}_a = 0, \quad \nabla \psi \cdot \vec{n} = 0, \quad \vec{A} \cdot \vec{n} = 0. \quad (\text{S9})$$

Hence the steady-state solutions of Eqs. (S7) and (S8) are determined by \vec{A} , d/λ , and κ , where d is the film thickness.

To solve Eqs. (S7)–(S9), COMSOL Multiphysics 5.1 was used. We closely followed the implementation introduced in Ref. 102. The general form of partial differential equations in COMSOL Multiphysics is

$$\mathbf{e}_a \frac{\partial^2 \mathbf{u}}{\partial t^2} + \mathbf{d}_a \frac{\partial \mathbf{u}}{\partial t} + \nabla \cdot \mathbf{\Gamma} = \mathbf{f}. \quad (\text{S10})$$

All geometries were assumed to be two-dimensional systems on the xy plane. \vec{H}_a is assumed to be along the z direction. In this case, $\mathbf{u} = (u_1, u_2, u_3, u_4, u_5)^T$, where T is the transpose. The variables are given by $u_1(x, y, t) = \text{Re}(\psi(x, y, t))$, $u_2(x, y, t) = \text{Im}(\psi(x, y, t))$, $u_3(x, y, t) = A_x(x, y, t)$, and $u_4(x, y, t) = A_y(x, y, t)$, respectively. To satisfy the boundary conditions, we need five differential equations. Thus, an auxiliary variable u_5 is introduced, which is always zero.

In Eq. (S10), \mathbf{e}_a is a zero matrix. Others can be written as

$$\mathbf{d}_a = \begin{bmatrix} 1 & 0 & 0 & 0 & 0 \\ 0 & 1 & 0 & 0 & 0 \\ 0 & 0 & \sigma_n & 0 & 0 \\ 0 & 0 & 0 & \sigma_n & 0 \\ 0 & 0 & 0 & 0 & 0 \end{bmatrix}, \quad \mathbf{\Gamma} = \begin{bmatrix} [-\partial_x u_1/\kappa^2, -\partial_y u_1/\kappa^2]^T \\ [-\partial_x u_2/\kappa^2, -\partial_y u_2/\kappa^2]^T \\ [0, \partial_x u_4 - \partial_y u_3 - \mu_0 H_a]^T \\ [-\partial_x u_4 + \partial_y u_3 + \mu_0 H_a, 0]^T \\ [u_3, u_4]^T \end{bmatrix},$$

$$\mathbf{f} = \begin{bmatrix} (\partial_x u_3 + \partial_y u_4)u_2/\kappa + 2(u_3 \partial_x u_2 + u_4 \partial_y u_2)/\kappa - (u_3^2 + u_4^2)u_1 + u_1 - (u_1^2 + u_2^2)u_1 \\ -(\partial_x u_3 + \partial_y u_4)u_1/\kappa - 2(u_3 \partial_x u_1 + u_4 \partial_y u_1)/\kappa - (u_3^2 + u_4^2)u_2 + u_2 - (u_1^2 + u_2^2)u_2 \\ (u_1 \partial_x u_2 - u_2 \partial_x u_1)/\kappa - (u_1^2 + u_2^2)u_3 \\ (u_1 \partial_y u_2 - u_2 \partial_y u_1)/\kappa - (u_1^2 + u_2^2)u_4 \\ \partial_x u_3 + \partial_y u_4 + u_5 \end{bmatrix}.$$

The boundary conditions were implemented using “zero flux” $-\vec{n} \cdot \mathbf{\Gamma} = \mathbf{G}$, where $\mathbf{G} = [0, 0, 0, 0, 0]^T$.

Setting proper initial values allows us to imitate cooling procedures, and consequently, to obtain the Bean-Livingston surface barrier naturally from the GL equations. All simulations shown in the main text were obtained with the initial condition for the zero-field cooling procedure: we set the initial condition as $u_1 = 1$, $u_2 = u_3 = u_4 = u_5 = 0$.

For Fig. 6, κ is 10 and the width of the slab along the x axis is 10λ . We apply a periodic boundary condition on the z axis, and the distance between the two boundaries is 2λ .

The mesh size is $\lambda_0/20$ for Fig. 4 and $\lambda_0/100$ for Fig. 6.

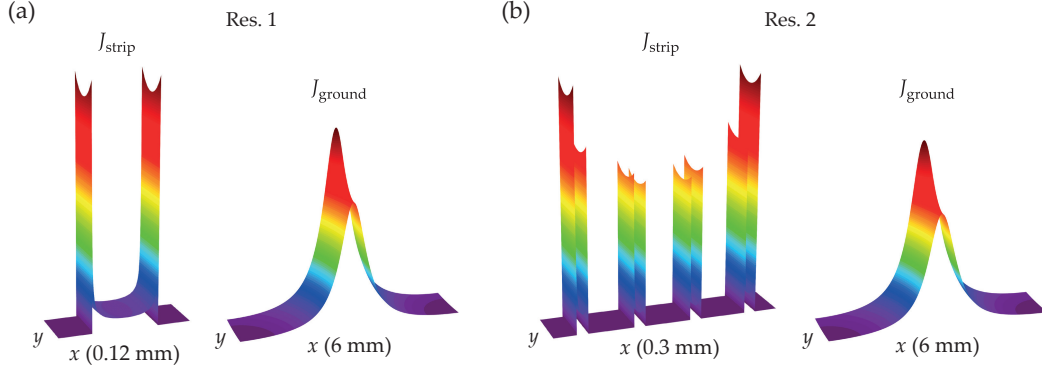


Figure S1: Numerically calculated microwave current density distribution of Res. 1 and 2. We assume the strips and the ground plane have the same penetration depth of $\lambda = 52$ nm. Both J_{strip} and J_{ground} are on an arbitrary scale; in practice, J_{ground} is orders of magnitude lower than J_{strip} . The numbers in parenthesis indicate the range of the plot.

S2 Microwave Current Density Distribution and Stored Electromagnetic Energy

To calculate the microwave current density distribution and the electromagnetic energy of our resonator, the London equations needed to be incorporated into Maxwell's equations. This was achieved by parameterizing the penetration depth via the complex conductivity (Eq. (8)).¹⁰³ As our resonators are straight strips, we did not need to consider the axis along the strip (z axis). By considering only the xy plane, we were able to simulate the entire cross section of the resonator packages.

The calculations were carried out using COMSOL Multiphysics 5.1 (AC/DC module). For the strips and the ground plane, the mesh sizes varied from $d/200$ to 0.5 mm. We confirmed our method by calculating several analytically solvable geometries¹⁰⁴ and the geometry of Ref. 103.

The microwave current density distribution of the strips J_{strip} and the ground plane J_{ground} of Res. 1 and 2 are shown in Fig. S1. The calculations show that the ratio of J_z^2 between the center of the strip, and the edges are about 400:1 and 100:1 for Res. 1 and 2 ($\lambda = 52$ nm), about 10:1 for Res. 3 ($\lambda = 162$), and about 800:1 for Res. 4 ($\lambda = 43$).

For all calculations, the value of λ for the strip and the ground plane was kept the same. This is a reasonable assumption, because the penetration depth dependence of integrated J_{ground}^2 is weak: J_{ground}^2 changes only about 4% from $\lambda = 50$ nm to 1000 nm.

S3 Loss Parameters for Quasiparticle Generation

In this section, we explain how to extract the loss parameters associated with quasiparticle generation from Fig. 4.

1. Calculate n_s as a function of H_{\parallel} by solving the GL equations as described in Sec. S1; λ_0 and κ are required for this step.
2. Once we have $n_s(H_{\parallel})$, $\lambda(H_{\parallel})$ is obtained by

$$\left(\frac{\lambda_0}{\lambda}\right)^2 = \frac{n_s(H_{\parallel})}{n_s(0)}. \quad (\text{S11})$$

Equation (S11) is derived from Eq. (8). Once λ is known, J_{strip} and L_{mag} are calculated as described in Sec. S2.

3. f^{-2} is reconstructed theoretically using Eqs. (4)–(8); H_c is required for this step.
4. Repeat Steps 1–3 until theoretical f^{-2} is sufficiently close to the experimental results. Then, λ_0 , κ , and H_c are determined.
5. Using $n_s(H_{\parallel})$ from the f^{-2} data, $Q_{0,\text{fit}}$, $\rho_{n,\text{fit}}$, and β are determined using a similar procedure with Q^{-1} . In order to calculate Q^{-1} , the following expression for $\sigma_{\text{tf},1}$ was used, which is based on Eq. (10):

$$\sigma_{\text{tf},1} = \left[1 - \frac{n_s(H_{\parallel})}{n_s(0)}\right]^{\beta} \frac{1}{\rho_{n,\text{fit}}}.$$

We remark that $\sigma_{\text{tf},1} \ll \sigma_{\text{tf},2}$ for most of the magnetic field range and $\rho_{\text{tf},2} = \sigma_{\text{tf},2}/(\sigma_{\text{tf},1}^2 + \sigma_{\text{tf},2}^2)$. As a result, $\rho_{n,\text{fit}}$ and β contribute to f^{-2} very little, and one can fit f^{-2} first. Note that a log-linear plot should be used, as shown in Fig. 4(a). The fitting for Fig. 4(b) was also done using the Q^{-1} vs. H_{\parallel} plot in a log-linear scale. The reason is that, although the changes to f^{-2} and Q^{-1} at low fields are small, they are crucial to obtain accurate loss parameters.

A crude description of the role of each fitting parameter is as follows: The curvature of n_s below the vortex penetration field is determined mostly by λ_0 , above the vortex penetration field the curvature is determined by κ . H_c scales n_s along the H_{\parallel} -axis. For Q^{-1} , β determines the curvature, A_n adjusts the scale along the Q^{-1} axis, and $Q_{0,\text{fit}}$ is the intercept on the Q axis in Fig. 4(b).

During the calculations, the ground plane's contribution was assumed negligible, hence λ_0 in Eq. (S11) is the zero-field penetration depth of the strips. The reason is that ground plane's contribution to the microwave current density is just a few percent. If the ground plane becomes normal prior to the strips, then its contribution might be comparable to that of the strips. To avoid such a complication, we kept the film thickness of the ground plane the same as that of the strips. As the ground plane is dirtier than the strips (see Table I and Sec. S5), its upper critical field is expected to be higher.

S4 Loss Parameters for Vortex Motion

In this section, we explain how to determine the loss parameters associated with vortex motion.

For the data taken after the heat-pulsing procedure, the procedure is more straightforward than that described in Sec. S3 because a homogeneous vortex distribution results in the complex resistivity proportional to H_{\perp} (Eq. (13)).

Using equations Eqs.(1)–(6), (12), and (13), we find:

$$\frac{f^{-2} - f_{\text{bg}}^{-2}}{f_{\text{bg}}^{-2}} = \frac{L - L_{\text{bg}}}{L_{\text{bg}}} \approx \frac{\Phi_0 B_{\perp}}{\eta} \frac{\omega/\omega_{\text{eff}}(1 - \epsilon)}{1 + (\omega/\omega_{\text{eff}})^2} \frac{1}{\omega} \frac{\int_{\text{sc}} |J_{\text{mw}}(x, y, \lambda)|^2 dx dy}{\int_{\text{all}} \mu_0 |H_{\text{mw}}(x, y, \lambda)|^2 dx dy}, \quad (\text{S12})$$

$$Q^{-1} - Q_{\text{bg}}^{-1} = \frac{P_{\text{diss}}}{\omega U_{\text{em}}} \approx \frac{\Phi_0 B_{\perp}}{\eta} \frac{(\omega/\omega_{\text{eff}})^2 + \epsilon}{1 + (\omega/\omega_{\text{eff}})^2} \frac{1}{\omega} \frac{\int_{\text{sc}} |J_{\text{mw}}(x, y, \lambda)|^2 dx dy}{\int_{\text{all}} \mu_0 |H_{\text{mw}}(x, y, \lambda)|^2 dx dy}, \quad (\text{S13})$$

where $L_{\text{bg}} \equiv L(H_{\parallel} = H_{\text{bg}}, \theta = 0)$.

If vortex motion contributes dominantly to the complex resistivity, i.e., $[\rho_{\text{tf},i}(H_{\perp}) - \rho_{\text{tf},i}(0)] \ll \rho_{\text{vm},i}$, and ϵ is negligibly small, then we can extract the r -parameter using Eqs. (S12) and (S13):⁶⁶

$$r(H_{\perp}) \equiv \frac{\rho_{\text{vm},2}(H_{\perp})}{\rho_{\text{vm},1}(H_{\perp})} = \frac{(f^{-2} - f_{\text{bg}}^{-2})/f_{\text{bg}}^{-2}}{Q^{-1} - Q_{\text{bg}}^{-1}} \approx \frac{\omega_{\text{p}}}{\omega}. \quad (\text{S14})$$

Using Eq. (S14), the r -parameter of each data point can be obtained. Once we have r , we can obtain $\omega_{\text{p}} (= r\omega)$. For Table III, we used the average r value for all HP data points using the ratio between the slopes of $(f^{-2} - f_{\text{bg}}^{-2})/f_{\text{bg}}^{-2}$ and $Q^{-1} - Q_{\text{bg}}^{-1}$; the slopes were obtained by linear fitting. (For Res. 3, the zero-field cooling data above 14 mT were used because of the absence of the heat-pulsing data.)

Here, η can be calculated using either Eq. (S12) or (S13); we used Eq. (S12), because the measurement accuracy of f is better than that of Q .

$$\eta \approx \frac{\mu_0 H_{\perp}}{(f^{-2} - f_{\text{bg}}^{-2})/f_{\text{bg}}^{-2}} \frac{\int_{\text{sc}} |J_{\text{mw}}(x, y, \lambda_{\text{bg}})|^2 dx dy}{\int_{\text{all}} \mu_0 |H_{\text{mw}}(x, y, \lambda_{\text{bg}})|^2 dx dy} \frac{\Phi_0}{\omega} \frac{1}{r + r^{-1}}, \quad (\text{S15})$$

where $\lambda_{\text{bg}} \equiv \lambda(H_{\parallel} = H_{\text{bg}}, \theta = 0)$. In Eq. (S15), the second fraction was estimated by numerical calculation (see Sec. S2), and remaining fractions were given by experimental results. Similar to the case of r , the inverse of the slope of $(f^{-2} - f_{\text{bg}}^{-2})/f_{\text{bg}}^{-2}$ was used as the first fraction. Then, k_{p} is obtained using the relation $k_{\text{p}} = \eta\omega_{\text{p}}$ ^{60,61,63,64}.

Lastly, we argue why the vortex creep parameter ϵ is negligible for estimating ω_{p} , η , and k_{p} . The r -parameter from a measurement gives the upper bound of the vortex creep factor ϵ_{max} :⁶³

$$\epsilon_{\text{max}}(r) = 1 + 2r^2 - 2r\sqrt{1 + r^2}. \quad (\text{S16})$$

At 4.2 K, we obtained $r = 2.3$ for Res. 1, resulting in $\epsilon_{\text{max}} = 0.044$ from Eq. (S16). According to the Coffey–Clem model, ϵ is given by $\epsilon = [I_0(U_{\text{p}}/2k_{\text{B}}T)]^{-2}$, where I_0 is the modified Bessel function of the first kind, U_{p} is the height of the pinning potential, k_{B} is the Boltzmann constant, and T is the temperature. Then, $\epsilon_{\text{max}} = 0.044$ corresponds to the lower bound of the pinning potential $U_{\text{p},\text{min}} = 25$ K. Based on this, ϵ_{max} at 100 mK is expected to be negligible. A similar conclusion holds for other resonators.

S5 Niobium Thin Film Growth and Characterization

The films on wafers A and B were grown in the Omicron EVO-50 Sputter System. The base pressure was held in the order of 10^{-10} mBar. Prior to the deposition, we chemically cleaned the substrate, first in acetone and isopropanol solvents, followed by the standard clean 1 (SC1) process.¹⁰⁵ The substrate was next heated *in situ* to 1000 °C, while the chamber pressure was kept stable. Heat transfer into the transparent sapphire substrate was provided by a detachable molybdenum disc. Substrate cleaning is crucial to reduce surface losses.^{106,107}

After substrate cleaning, thin films were sputtered at elevated temperatures.¹⁰⁸ First, a niobium film, used as the ground plane, was grown at 770 °C, while the molybdenum piece was used to transfer the heat to the substrate. Next, the molybdenum disc was detached and the substrate was flipped (all *in situ*) to grow the film for the strips. Post-deposition heat is known to reconstruct and change the crystalline orientation of niobium thin films.¹⁰⁹ Therefore, the film was grown at 550 °C at this stage, to minimize the reconstruction of the ground plane. The deposition rate and Ar pressure were maintained at about 1.7 Å/s and 2×10^{-3} mBar, respectively, during the growth of the films on wafers A and B.

The films on wafer C were grown in the AJA ATC Orion Series Sputtering System. The base pressure was about 1×10^{-8} mbar. The substrate was first Ar-sputter cleaned for 5 min under substrate bias at 50 W RF power, 7×10^{-3} mbar Ar pressure, and 30 sccm of Ar flow. Next, we annealed the substrate at 700 °C for 1 h and then let it cool down for 7 h in a vacuum, which is long enough to ensure that the substrate reaches room temperature.

The annealing step was then followed by the deposition of the film for the strips. Afterwards, we flipped the wafer to grow the ground plane. For the ground plane, the substrate was only Ar-sputtered. Pre-deposition annealing was skipped to avoid heating the already existing film for the resonators. Both films on wafer C were deposited at room temperature; the deposition rate was around 0.6 Å/s, and Ar pressure was maintained at 4×10^{-3} mbar.

The thickness of each film was determined by fitting X-ray reflection intensity curves from grazing incident X-ray beams. The crystal orientation was obtained through the high-resolution X-ray diffraction pattern and the azimuthal X-ray diffraction data (ϕ -scan). For wafers A and B, the out-plane crystalline orientation of the films for the strips is along the (111) direction (Table I). Such an orientation is previously reported as a result of growth at elevated substrate temperatures.^{109,110} Depending on the substrate temperature, mixed orientations are also possible as observed in the ground plane of wafer A.¹¹¹

The film quality was characterized by transport measurements using the van der Pauw method¹¹² on 4.7 mm \times 4.7 mm square chips diced before resonator fabrication. A criterion $0.5R_n$, where R_n is the normal state resistance, was used to define T_c .